Adhesive nonlinearity in Lamb-wave-based structural health monitoring systems

2017 Smart Mater. Struct. 26 025019

(http://iopscience.iop.org/0964-1726/26/2/025019)

IOP Publishing Smart Materials and Structures
Smart Mater. Struct. 26 (2017) 025019 (17pp) doi:10.1088/1361-665X/26/2/025019

Adhesive nonlinearity in Lamb-wave-based structural health monitoring systems

Shengbo Shan, Li Cheng and Peng Li

Department of Mechanical Engineering, The Hong Kong Polytechnic University, Kowloon, Hong Kong, People's Republic of China

E-mail: li.cheng@polyu.edu.hk

Received 21 July 2016, revised 30 September 2016
Accepted for publication 1 November 2016
Published 30 December 2016

Abstract

Structural health monitoring (SHM) techniques with nonlinear Lamb waves have gained wide popularity due to their high sensitivity to microstructural changes for the detection of damage precursors. Despite the significant progress made, various unavoidable nonlinear sources in a practical SHM system, as well as their impact on the detection, have not been fully assessed and understood. For the real-time and online monitoring, transducers are usually permanently bonded on the structure under inspection. In this case, the inherent material nonlinear properties of the bonding layer, referred to as adhesive nonlinearity (AN), may create undesired interference to the SHM system, or even jeopardize the damage diagnosis if they become serious. In this paper, a nonlinear theoretical framework is developed, covering the process of wave generation, propagation and sensing, with the aim of investigating the mechanism and characteristics of AN-induced Lamb waves in plates, which potentially allows for further system optimization to minimize the influence of AN. The model shows that an equivalent nonlinear normal stress is generated in the bonding layer due to its nonlinear material behavior, which, through its coupling with the system, is responsible for the generation of second harmonic Lamb waves in the plate, subsequently resulting in the nonlinear responses in the captured signals. With the aid of the finite element (FE) modeling and a superposition method for nonlinear feature extraction, the theoretical model is validated in terms of generation mechanism of the AN-induced wave components as well as their propagating characteristics. Meanwhile, the influence of the AN is evaluated by comparing the AN-induced nonlinear responses with those caused by the material nonlinearity of the plate, showing that AN should be considered as a non-negligible nonlinear source in a typical nonlinear Lamb-wave-based SHM system. In addition, the theoretical model is also experimentally validated in terms of the frequency tuning characteristics of the AN-induced wave components. A fairly good agreement is found among the theoretical model, FE model and the experiments, thus confirming the theoretically predicted AN-induced wave generation mechanism and their characteristics.

Keywords: structural health monitoring, nonlinear guided waves, adhesive nonlinearity

(Some figures may appear in colour only in the online journal)

1. Introduction

The presence of the damage in engineering structures, in whatever form it is manifested, can significantly jeopardize their operation and safety without timely awareness. Therefore, early detection of the initial damage in real time becomes important to enhance the safety and extend the residual lifetime of structures in service, as well as to effectively drive down the exorbitant maintenance cost [1]. This urgent need hatches out the concept of structural health monitoring (SHM), which aims at the online damage diagnosis with built-in transducers [1–3]. Among various SHM approaches, the one based on guided waves is probably one of the most popular methods due to its appealing features like low energy consumption, far-reaching detection area and high sensitivity to damage [1, 3–6].

Conventional solutions based on guided waves focus on the damage scattering properties of the waves, which are classified in the category of linear SHM methods [7]. It is widely accepted that linear features of the guided waves are good indicators for macro-scale defects, typically in the order of millimeter range [8, 9]. For practical applications, however, the appearance of the macro-scale damage may lead to rapid disruption of the structure. Therefore, early detection of small and incipient changes is highly desirable, which linear solutions can hardly cope with. In this context, nonlinear guided waves, which exhibit higher sensitivity to microstructural changes through the exploration of the second harmonic generation, started to attract more and more attentions in recent years [10–12].

Generally speaking, the second harmonic guided waves (Lamb waves of our specific interest) can be generated by both crack-induced nonlinearity [13, 14] and material nonlinearity [15, 16]. With the main focus on the nonlinear properties of the waveguides, theoretical basis revealing the mechanism of the generation of second harmonic Lamb waves has been well developed [15–19]. These investigations show that two conditions are necessary for the cumulative second harmonic generation: phase velocity matching and non-zero power flux, resulting in a few SHM-usable mode pairs at some specific frequencies. These theoretical findings provide the guidance for the application of the nonlinear Lamb waves in SHM, including the selection of excitation frequencies, the design of transducers and so on [17, 18, 20]. For example, Hong *et al* [21] managed to extract the damage information from the second-harmonic Lamb waves to locate fatigue damage at a rivet hole with surface-bonded PZT discs (PZT denotes PbZr–TiO_3). Rauter and Lammering [22] detected fatigue damage in a composite plate using the second harmonic components of Lamb waves with piezoelectric transducers. Those previous experiments demonstrate that the nonlinear Lamb-wave-based SHM technique has great potential for the detection of damage precursors in many engineering applications.

More recently, it has been reported that strong cumulative second harmonic S_0 wave components can also be generated by the primary S_0 Lamb waves in plates at relatively low-frequency range as long as the phase velocities of the primary and secondary waves approximately match [23]. This allows the use of lower excitation frequencies for the cumulative second harmonic generation, which is preferable in real applications because the signal complexity and the requirements for the experimental equipment can be significantly reduced. In addition, the condition of approximate phase velocity matching gives the flexibility for the choice of excitation frequencies.

However, in a typical nonlinear Lamb-wave-based SHM system with transducers permanently bonded on the host structures, there might be other non-negligible nonlinear sources apart from the nonlinearity of the waveguides, like instrument nonlinearity, that of the transducers and the bonding layers. The influence of these undesired nonlinear sources on the SHM method needs to be evaluated before meaningful and convincing diagnosis conclusions can be reached. Of our specific interest, the nonlinearity associated with the bonding layers will be investigated. Similar to the crack-induced nonlinearity and material nonlinearity of the waveguides, two main mechanisms are responsible for the generation of the second harmonic waves associated with bonding layers: debonding and nonlinear material properties of bonding layers. For the former, relevant research has been carried out through both finite element (FE) analyses and experimental investigations [24]. Results demonstrate that strong second harmonics of Lamb waves can be generated when transducers are partially debonded. For the latter, the material nonlinearity of the bonding layers is referred to as adhesive nonlinearity (AN) in this paper. Although it is well accepted that the properties of the adhesive have a significant influence on the linear Lamb-wave-based SHM methods [25–27], the influence of the AN on the nonlinear SHM methods has not been fully investigated so far and this motivated the current work. The evaluation of the AN is challenging mainly for several reasons. First, it is a complex coupling problem with the transducers bonded to the host structure, which requires appropriate assumptions in the model development. Second, references on the acquisition of the nonlinear elastic parameters of adhesives are scarce, or even inexistent in some aspects, in the literature due to their complex viscoelastic properties. Third, most existing signal processing methods used in the nonlinear SHM like fast Fourier transform [28], short time Fourier transform [21] and wavelet transform [23] are unable to extract the original nonlinear responses in the time domain, which can hardly make the model validation process convincing.

In this study, we propose a coupled model to investigate the mechanism of the AN and assess the characteristics of the AN-induced second harmonic Lamb waves, which can potentially be used for further system optimization to minimize the influence of AN. The proposed model is inspired by some existing linear Lamb-wave-based SHM models [1, 29–31]. Particularly, the shear-lag model developed by Giurgiutu *et al* is highlighted, which has been successfully applied to predict the phenomenon of frequency tuning [31]. In the present study, the shear-lag model is extended to form a nonlinear framework through a perturbation method. The proposed model combines the entire process of Lamb wave generation, propagation and sensing with the AN introduced to both actuator-plate and sensor-plate interfaces using the nonlinear elastic properties of the adhesive. The theoretical model allows calculating the linear and nonlinear responses in terms of the voltage output of the PZT sensors in the time domain. Model validation is carried out using both FE and experimental results. For FE validation, a FE model is established with the experimentally measured nonlinear elastic parameters of the adhesive. The nonlinear responses are extracted by the superposition method which allows separating the linear and nonlinear parts of the response and validating the model in the perspective of propagating characteristics of nonlinear wave components. In addition, the influence of the AN is analyzed and evaluated. Experiments are carried out to further ascertain the frequency tuning characteristics of nonlinear S_0 Lamb wave components.

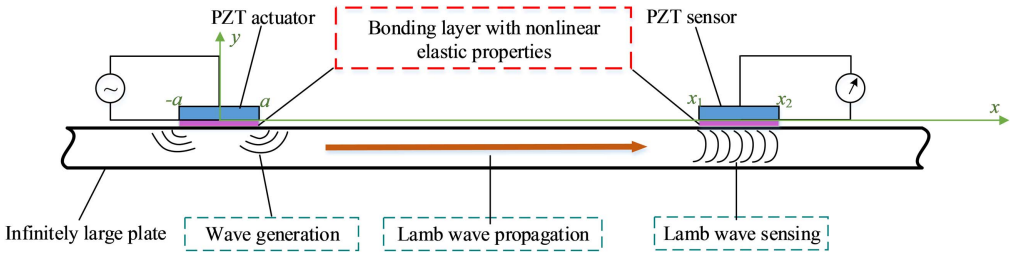

Figure 1. Sketch of the theoretical model.

2. Theoretical model

The model consists of an infinite plate incorporating the three modules, usually present in a typical Lamb-wave-based SHM system: wave generation, propagation and sensing, as shown in figure 1. PZT transducers, used either as actuators or sensors, are bonded on the surface of the plate under inspection through adhesive layers. The adhesive ensuring the PZT-plate interactions is assumed to have nonlinear elastic properties. By contrast, the piezoelectric transducers and the plate are considered as linear waveguides in terms of their elastic and piezoelectric properties. For Lamb waves generated by the PZT discs, the small deformation assumption is adopted throughout the analyses. In principle, AN exists in both the actuator-plate and sensor-plate interfaces. The nonlinearity at the actuation area is referred to as the actuator adhesive nonlinearity (AAN) while the one at the sensing area the sensor adhesive nonlinearity (SAN). In addition, only the second harmonic wave components are considered due to their extensive use in most nonlinear Lamb-wave-based SHM methods.

2.1. Nonlinear material elastic properties

The nonlinear material behavior of the adhesive is first evaluated. Similar to previous relevant studies, the constitutive equation of the adhesive is expressed with the Landau–Lifshitz model [17]:

$$\mathbf{T} = \lambda \mathrm{tr}[\mathbf{E}] + 2\mu\mathbf{E} + C(\mathrm{tr}[\mathbf{E}])^2\mathbf{I} + B\mathrm{tr}[\mathbf{E}^2]\mathbf{I} + 2B\mathrm{tr}[\mathbf{E}]\mathbf{E} + A\mathbf{E}^2, \tag{1}$$

where λ and μ are Lamé constants, while A, B, C are defined as the third-order elastic constants (TOECs). The operation tr() denotes the trace of a matrix. $\mathbf{T}$ is the second Piola–Kirchhoff stress tensor and $\mathbf{E}$ the Lagrangian strain tensor, whose components can be written as

$$\varepsilon_{ij} = \frac{1}{2}\left(\frac{\partial X_i}{\partial D_j} + \frac{\partial X_j}{\partial D_i} + \frac{\partial X_k}{\partial D_j}\frac{\partial X_k}{\partial D_i}\right), \tag{2}$$

where $X = [u\ v]^{\mathrm{T}}$ is the displacement vector and D the spatial directions. By applying the small deformation assumption, the nonlinear term $\frac{\partial X_k}{\partial D_j}\frac{\partial X_k}{\partial D_i}$ in the equation which corresponds to the geometric nonlinearity (GN) is first omitted so that the Lagrangian strains retreat to engineering strains [32]. By the same token, the nominal stress is used instead of the second Piola–Kirchhoff stress in the following analyses. The influence of the GN will be numerically evaluated in the subsequent section on FE validation.

Two typical types of material behavior are considered: uniaxial tension and pure shearing. During the uniaxial tension process, the stress–strain relationship writes

$$T_1 = E\varepsilon_1 + \left[C\left(\frac{\mu}{\lambda+\mu}\right)^2 + B\left(1 + 2\left(\frac{\lambda}{2(\lambda+\mu)}\right)^2\right) + 2B\left(\frac{\mu}{\lambda+\mu}\right) + A\right]\varepsilon_1{}^2, \tag{3}$$

where E is the Young's modulus of the material. In the pure shearing deformation in the x_1–x_2 plane, the nonlinear stress–strain relationship writes

$$T_{12} = 2\mu\varepsilon_{12} + \left[2A\left(\frac{\lambda(3B+A)}{\mu(3\lambda+2\mu)} - \frac{2B+A}{2\mu}\right) - 2B\left(\frac{6B+2A}{3\lambda+2\mu}\right)\right]\varepsilon_{12}{}^3. \tag{4}$$

Detailed derivations can be found in appendix A. It is worth noting that only the linear and third-harmonic terms of the shear strain appear in equation (4). As the focus of this work is on the second harmonics, the third-order term is omitted and the shear stress-strain relation can be simplified as

$$T_{12} = \mu\gamma_{12}, \tag{5}$$

where γ_{12} is the commonly-used engineering shear strain, which is related to the shear strain component by $\gamma_{12} = 2\varepsilon_{12}$.

In the pure shearing process, equation (A.15), which represents the stress–strain relation in the x_1 direction, can be described as:

$$T_e = -\frac{(2B+A)\gamma_{12}{}^2}{4} = \lambda(\varepsilon_1+\varepsilon_2+\varepsilon_3) + 2\mu\varepsilon_1. \tag{6}$$

The above equation indicates that an equivalent second-harmonic normal stress, T_e, is generated mainly through normal strain ε_1. This process is considered to be responsible for the AN-induced second harmonic generation, to be validated in the subsequent analyses.

2.2. Wave generation

As the first module in the theoretical model, the wave generation mechanism is investigated by extending the classic shear-lag model to the nonlinear one, named as nonlinear shear-lag model. Previous nonlinear studies indicate the

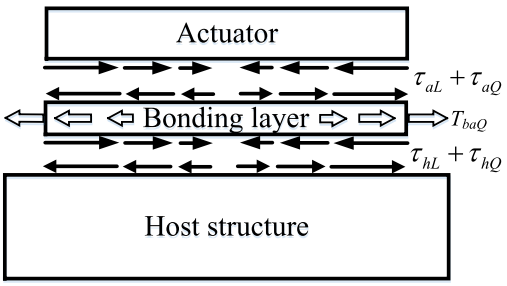

Figure 2. Sketch of the wave actuating problem.

validity of the assumption that the amplitude of the second harmonic components due to the material nonlinearity is much smaller than that of the fundamental waves [17]. Consequently, the problems characterized by the nonlinear shear-lag model can be decoupled to linear and nonlinear problems through the perturbation method. In addition, other assumptions from the classic shear-lag model are adopted in this theoretical framework, namely, (1) the problem is treated as a one-dimensional problem, that is, only the d_{31} effect of the piezoelectric element is responsible for the generation of Lamb waves. (2) Inertial terms of the PZT, as well as these of the bonding layer and plate are neglected in the model, thus limiting the accuracy of the model up to certain frequencies, which concurs with our focus on the relatively low-frequency range. (3) The deformation of the bonding layer is simplified as pure shearing in the linear case, whilst an additional equivalent normal stress is generated in the bonding layer in the nonlinear case.

The nonlinear variables can be expressed as

$$V = V_L(x)f(t) + V_Q(x)g(t) \tag{7}$$

in which V is a variable which can be u for displacement, ε and γ for normal and shear strains or σ and τ for normal and shear stresses, respectively. The subscripts L and Q denote the linear and quadratic terms, respectively. $f(t)$ and $g(t)$ are time-dependent terms. In this specific case, as no inertial terms are considered, the two terms are related by $g(t) = (f(t))^2$. In the subsequent derivation, the time-dependent terms $f(t)$ and $g(t)$ will be omitted for the sake of simplicity.

The nonlinear shear-lag model is established by formulating the governing equations including constitutive, geometric and equilibrium equations of the actuator, bonding layer and the host structure, respectively. A sketch showing the force transmissions in the model is given in figure 2.

For the actuator, the three governing equations are described as

$$\sigma_{\mathrm{a}} = \sigma_{\mathrm{a}L} + \sigma_{\mathrm{a}Q} = E_{\mathrm{a}}(\varepsilon_{\mathrm{a}L} + \varepsilon_{\mathrm{a}Q} - \varepsilon_{\mathrm{ISA}}), \tag{8}$$

$$\varepsilon_{\mathrm{a}} = \varepsilon_{\mathrm{a}L} + \varepsilon_{\mathrm{a}Q} = \frac{\mathrm{d}(u_{\mathrm{a}L} + u_{\mathrm{a}Q})}{\mathrm{d}x}, \tag{9}$$

$$t_{\mathrm{a}}E_{\mathrm{a}}(\varepsilon_{\mathrm{a}L}{}' + \varepsilon_{\mathrm{a}Q}{}') - (\tau_{\mathrm{a}L} + \tau_{\mathrm{a}Q}) = 0, \tag{10}$$

where the subscript a stands for the actuator. E and t are the Young's modulus and thickness of the PZT actuators respectively. $\varepsilon_{\mathrm{ISA}}$ denotes the linear piezoelectric-induced strain, described as

$$\varepsilon_{\mathrm{ISA}} = \frac{d_{31\mathrm{a}}V_{\mathrm{in}}}{t_{\mathrm{a}}}, \tag{11}$$

where d_{31} is the piezoelectric constant and V_{in} the input voltage. Similarly, the governing equations for the host structure can be written as

$$\sigma_{\mathrm{h}} = \sigma_{\mathrm{h}L} + \sigma_{\mathrm{h}Q} = E_{\mathrm{h}}(\varepsilon_{\mathrm{h}L} + \varepsilon_{\mathrm{h}Q}), \tag{12}$$

$$\varepsilon_{\mathrm{h}} = \varepsilon_{\mathrm{h}L} + \varepsilon_{\mathrm{h}Q} = \frac{\mathrm{d}(u_{\mathrm{h}L} + u_{\mathrm{h}Q})}{\mathrm{d}x}, \tag{13}$$

$$t_{\mathrm{h}}E_{\mathrm{h}}(\varepsilon'_{\mathrm{h}L} + \varepsilon'_{\mathrm{h}Q}) + \alpha(\tau_{\mathrm{h}L} + \tau_{\mathrm{h}Q}) = 0, \tag{14}$$

where the subscript h represents the host structure. The coefficient α depends on the stress, strain, and displacement distributions across the plate thickness. In the low-frequency range, especially when only A_0 and S_0 modes of Lamb waves exist in the plate, α is set to 4 [31].

For the bonding layer, the governing equations can be expressed as

$$\tau_{\mathrm{ba}} = \tau_{\mathrm{ba}L} + \tau_{\mathrm{ba}Q} = G_{\mathrm{ba}}(\gamma_{\mathrm{ba}L} + \gamma_{\mathrm{ba}Q}), \tag{15}$$

$$\gamma_{\mathrm{ba}} = \gamma_{\mathrm{ba}Q} + \gamma_{\mathrm{ba}L} = \frac{(u_{\mathrm{a}L} + u_{\mathrm{a}Q}) - (u_{\mathrm{h}L} + u_{\mathrm{h}Q})}{t_{\mathrm{ba}}}, \tag{16}$$

$$t_{\mathrm{ba}}\frac{\mathrm{d}T_{\mathrm{ba}Q}}{\mathrm{d}x} + (\tau_{\mathrm{a}L} + \tau_{\mathrm{a}Q}) - (\tau_{\mathrm{h}L} + \tau_{\mathrm{h}Q}) = 0, \tag{17}$$

where the subscript ba denotes the bonding layer under the actuator. G is the shear modulus of the adhesive and $T_{\mathrm{ba}Q}$ is the equivalent nonlinear normal stress on the bonding layer. The shear stress of the bonding layer is related to that over the actuator-plate interface, given by

$$\frac{(\tau_{\mathrm{a}L} + \tau_{\mathrm{a}Q}) + (\tau_{\mathrm{h}L} + \tau_{\mathrm{h}Q})}{2} = \tau_{\mathrm{ba}L} + \tau_{\mathrm{ba}Q}. \tag{18}$$

If admitting that the amplitude of the quadratic terms is usually much smaller than their linear counterparts and all the quadratic terms in the governing equations being omitted, the problem will be reduced to the classic shear-lag model. Referring to the classic shear-lag solutions with the stress-free boundary conditions [1, 31], the linear shear stress distribution can be obtained as:

$$\tau_{\mathrm{a}L}(x) = \tau_{\mathrm{h}L}(x) = \tau_{\mathrm{ba}L}(x) = \frac{G_{\mathrm{ba}}\varepsilon_{\mathrm{ISA}}}{t_{\mathrm{ba}}\Gamma_{\mathrm{a}}}\frac{\sinh(\Gamma_{\mathrm{a}}x)}{\cosh(\Gamma_{\mathrm{a}}a)}, \tag{19}$$

where a is the half length of the actuator. Parameters ψ_{a} and Γ_{a} are defined as

$$\psi_{\mathrm{a}} = \frac{t_{\mathrm{h}}E_{\mathrm{h}}}{t_{\mathrm{a}}E_{\mathrm{a}}}, \tag{20}$$

$$\Gamma_{\mathrm{a}}{}^2 = \frac{G_{\mathrm{ba}}}{t_{\mathrm{ba}}t_{\mathrm{a}}E_{\mathrm{a}}}\frac{\alpha + \psi_{\mathrm{a}}}{\psi_{\mathrm{a}}}. \tag{21}$$

Based on equation (6), the equivalent nonlinear normal stress writes

$$\begin{aligned} T_{\mathrm{ba}Q} &= \frac{-(2B + A)\gamma_{\mathrm{ba}L}{}^2}{4} \\ &= \frac{-(2B + A)}{4}\left(\frac{\varepsilon_{\mathrm{ISA}}}{t_{\mathrm{ba}}\Gamma_{\mathrm{a}}}\frac{\sinh(\Gamma_{\mathrm{a}}x)}{\cosh(\Gamma_{\mathrm{a}}a)}\right)^2. \end{aligned} \tag{22}$$

According to the perturbation method, the nonlinear problem can then be constructed by eliminating all the linear terms from the governing equations from equations (8) to (18). Upon rearranging the equations, the differential equation in terms of the variable τ_{hQ} can be written as

$$\tau''_{\mathrm{h}Q} - {\Gamma_{\mathrm{a}}}^2\tau_{\mathrm{h}Q} = R\sinh(2\Gamma_{\mathrm{a}}x), \tag{23}$$

where R and P are two intermediate constants which can be expressed as

$$R = P\left(\frac{G_{\mathrm{ba}}}{E_{\mathrm{a}}t_{\mathrm{a}}t_{\mathrm{ba}}} - 2{\Gamma_{\mathrm{a}}}^2\right),\ P = \frac{(2B+A){\varepsilon_{\mathrm{ISA}}}^2}{4t_{\mathrm{ba}}\Gamma_{\mathrm{a}}(\cosh(\Gamma_{\mathrm{a}}a))^2}. \tag{24}$$

As the actuator and the host structure have stress-free boundaries, the final solution to this nonlinear problem writes

$$\begin{aligned}\tau_{\mathrm{h}Q} = &-\left(\frac{2R}{3{\Gamma_{\mathrm{a}}}^2} + P\right)\frac{\cosh(2\Gamma_{\mathrm{a}}a)}{\cosh(\Gamma_{\mathrm{a}}a)}\sinh(\Gamma_{\mathrm{a}}x)\\ &+ \frac{R}{3{\Gamma_{\mathrm{a}}}^2}\sinh(2\Gamma_{\mathrm{a}}x).\end{aligned} \tag{25}$$

Details of the equation derivation are provided in appendix B.

2.3. Wave propagation

The second module in the model is the wave propagation. In this work, only A_0 and S_0 modes of Lamb waves which propagate in a linear isotropic aluminum plate will be considered in the low-frequency range. Once the shear stress distributions are obtained, the corresponding strains of Lamb waves subjected to a harmonic excitation can be obtained as [1]

$$\begin{aligned}{\varepsilon_L}^H = &\frac{1}{2G_{\mathrm{h}}}\frac{\tilde{\tau}_{\mathrm{h}}(\xi_{\mathrm{S}0})N_S(\xi_{\mathrm{S}0})}{D_S'(\xi_{\mathrm{S}0})}\mathrm{e}^{\mathrm{i}(\xi_{\mathrm{S}0}x-\omega t)}\\ &+ \frac{1}{2G_{\mathrm{h}}}\frac{\tilde{\tau}_{\mathrm{h}}(\xi_{\mathrm{A}0})N_{\mathrm{A}}(\xi_{\mathrm{A}0})}{D_{\mathrm{A}}'(\xi_{\mathrm{A}0})}\mathrm{e}^{\mathrm{i}(\xi_{\mathrm{A}0}x-\omega t)},\end{aligned} \tag{26}$$

where ξ denotes the wave number for either A_0 and S_0 Lamb wave modes and G_{h} is the shear modulus of the host structure. Expressions for intermediate variables, N_A, N_S, D_A and D_S are:

$$N_{\mathrm{S}}(\xi_{\mathrm{S}0}) = \xi_{\mathrm{S}0}\eta^{\mathrm{S}}_{\mathrm{S}0}({\xi_{\mathrm{S}0}}^2 + {\eta^{\mathrm{S}}_{\mathrm{S}0}}^2)\cos(\eta^{P}_{\mathrm{S}0}d)\cos(\eta^{\mathrm{S}}_{\mathrm{S}0}d), \tag{27}$$

$$N_{\mathrm{A}}(\xi_{\mathrm{A}0}) = -\xi_{\mathrm{A}0}\eta^{\mathrm{S}}_{\mathrm{A}0}({\xi_{\mathrm{A}0}}^2 + {\eta^{\mathrm{S}}_{\mathrm{A}0}}^2)\sin(\eta^{P}_{\mathrm{A}0}d)\sin(\eta^{\mathrm{S}}_{\mathrm{A}0}d), \tag{28}$$

$$\begin{aligned}D_S(\xi_{\mathrm{S}0}) = &({\xi_{\mathrm{S}0}}^2 - {\eta^{\mathrm{S}}_{\mathrm{S}0}}^2)^2\cos(\eta^{P}_{\mathrm{S}0}d)\sin(\eta^{\mathrm{S}}_{\mathrm{S}0}d)\\ &+ 4\xi_{\mathrm{S}0}\eta^{\mathrm{S}}_{\mathrm{S}0}\eta^{P}_{\mathrm{S}0}\sin(\eta^{P}_{\mathrm{S}0}d)\cos(\eta^{\mathrm{S}}_{\mathrm{S}0}d),\end{aligned} \tag{29}$$

$$\begin{aligned}D_A(\xi_{\mathrm{A}0}) = &({\xi_{\mathrm{A}0}}^2 - {\eta^{\mathrm{S}}_{\mathrm{S}0}}^2)^2\cos(\eta^{P}_{\mathrm{S}0}d)\sin(\eta^{\mathrm{S}}_{\mathrm{S}0}d)\\ &+ 4\xi_{\mathrm{A}0}\eta^{\mathrm{S}}_{\mathrm{S}0}\eta^{P}_{\mathrm{S}0}\sin(\eta^{P}_{\mathrm{S}0}d)\cos(\eta^{\mathrm{S}}_{\mathrm{S}0}d),\end{aligned} \tag{30}$$

where

$$\begin{aligned}&{\eta^{\mathrm{P}}_{\mathrm{S}0}}^2 = \frac{\omega^2}{{c_{\mathrm{P}}}^2} - {\xi_{\mathrm{S}0}}^2,\ {\eta^{\mathrm{P}}_{\mathrm{A}0}}^2 = \frac{\omega^2}{{c_{\mathrm{P}}}^2} - {\xi_{\mathrm{A}0}}^2,\\ &{\eta^{\mathrm{S}}_{\mathrm{s}0}}^2 = \frac{\omega^2}{{c_{\mathrm{S}}}^2} - {\xi_{\mathrm{s}0}}^2,\ {\eta^{\mathrm{S}}_{\mathrm{A}0}}^2 = \frac{\omega^2}{{c_{\mathrm{S}}}^2} - {\xi_{\mathrm{A}0}}^2,\end{aligned} \tag{31}$$

where ω is the excitation frequency and c_{P} and c_{S} the wave speeds for the pressure wave and the shear wave, respectively. d is the half thickness of the plate. $\tilde{\tau}_{\mathrm{h}}$ is the Fourier transform of the shear stress distribution on the top surface of the host structure for either linear or nonlinear terms, which can be calculated by:

$$\begin{aligned}\tilde{\tau}_{\mathrm{h}L}(\xi) = &\frac{G_{\mathrm{ba}}\varepsilon_{\mathrm{ISA}}}{2t_{\mathrm{ba}}\Gamma_{\mathrm{a}}\cosh(\Gamma_{\mathrm{a}}a)}\left[\frac{1}{\Gamma_{\mathrm{a}} - \mathrm{i}\xi}\mathrm{e}^{(\Gamma_{\mathrm{a}}-\mathrm{i}\xi)x}\right.\\ &\left. - \frac{1}{-\Gamma_{\mathrm{a}} - \mathrm{i}\xi}\mathrm{e}^{(-\Gamma_{\mathrm{a}}-\mathrm{i}\xi)x}\right]\Bigg|_{-\mathrm{a}}^{\mathrm{a}},\end{aligned} \tag{32}$$

$$\begin{aligned}\tilde{\tau}_{\mathrm{h}Q}(\xi) = &-\left(\frac{R}{3{\Gamma_{\mathrm{a}}}^2} + \frac{P}{2}\right)\frac{\cosh(2\Gamma_{\mathrm{a}}a)}{\cosh(\Gamma_{\mathrm{a}}a)}\\ &\times\left[\frac{1}{\Gamma_{\mathrm{a}} - \mathrm{i}\xi}\mathrm{e}^{(\Gamma_{\mathrm{a}}-\mathrm{i}\xi)x} - \frac{1}{-\Gamma_{\mathrm{a}} - \mathrm{i}\xi}\mathrm{e}^{(-\Gamma_{\mathrm{a}}-\mathrm{i}\xi)x}\right]\Bigg|_{-a}^{a}\\ &+ \frac{R}{6{\Gamma_{\mathrm{a}}}^2}\left[\frac{1}{2\Gamma_{\mathrm{a}} - \mathrm{i}\xi}\mathrm{e}^{(2\Gamma_{\mathrm{a}}-\mathrm{i}\xi)x}\right.\\ &\left. - \frac{1}{-2\Gamma_{\mathrm{a}} - \mathrm{i}\xi}\mathrm{e}^{(-2\Gamma_{\mathrm{a}}-\mathrm{i}\xi)x}\right]\Bigg|_{-a}^{a}.\end{aligned} \tag{33}$$

From equation (26), the linear and quadratic responses in the frequency domain can be determined. It is worth noting that the calculation of the nonlinear response is based on the assumption that the AAN-induced second-harmonic Lamb waves propagate independently of the primary Lamb waves at their respective velocities.

In most SHM applications, tone-burst excitations are preferred as they can provide sufficient temporal information for damage diagnosis. Thus, the time-domain responses need to be calculated. Given a certain position x_0, the frequency response function, denoted by $G(\omega)$, can be obtained from equation (26). Subjected to an excitation signal $f_{\mathrm{e}}(t)$, the time-domain response in terms of the normal strain can be calculated as

$$\varepsilon(x_0, t) = \mathrm{IF}[F(f_{\mathrm{e}}(t)) \cdot G(\omega)], \tag{34}$$

where F() and IF() represent the direct and inverse Fourier transform, respectively. Finally, the temporal signals of the strains at any position can be obtained as $\varepsilon_{\mathrm{h}RL}$ for the linear response and ε_{hRQ} for the ANN-induced nonlinear response.

2.4. Wave sensing

At the last module in the model, the propagating Lamb waves are captured and converted to voltage signals by the surface-bonded piezoelectric sensor. Previous work showed that the sensor itself has negligible influence on the propagation the of Lamb waves [33]. This is used here as an additional assumption. Similar to the wave generation module, the output signal includes both linear and nonlinear components according to the perturbation method. More specifically, the nonlinear response will include both AAN-induced and SAN-induced components, presumably captured by the sensor

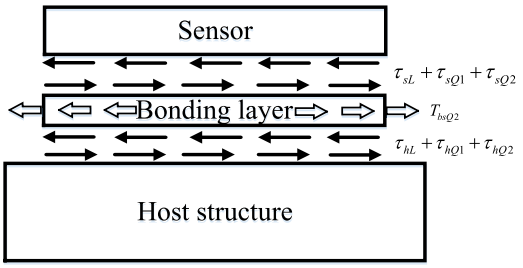

Figure 3. Sketch of the wave sensing problem.

independently. Physically, the former propagates at different speeds before reaching the sensor at different time instants, whilst the latter is mainly generated by the linear Lamb wave at the sensor position. Thus the wave sensing process can be divided into three individual problems: linear Lamb wave sensing (using notations with the subscribe L in the following analysis), linear wave sensing of AAN-induced wave components (with the subscript $Q1$) and nonlinear wave sensing of SAN-induced wave components (with the subscript $Q2$), as shown in figure 3.

As to the linear wave sensing part, the equilibrium equations of the piezoelectric sensor and the bonding layer can be written as

$$t_s E_s \varepsilon'_{sL} - \tau_{sL} = 0, \tag{35}$$

$$\tau_{sL} = \tau_{hL} = \tau_{bsL}, \tag{36}$$

where the subscripts s and bs stand for the sensor and bonding layer under the sensor, respectively. The constitutive and geometric equations of the sensor and bonding layer are analogous to those in the wave actuation case. The only difference lies in the absence of the piezoelectric term in the constitutive equation of the sensor, as

$$\sigma_{sL} = E_s \varepsilon_{sL}. \tag{37}$$

As the normal strain of the host structure is a known variable, the differential equation with respect to the normal strain of the sensor can be obtained by substituting the geometric and constitutive equations of the bonding layer into equation (35) as

$$\varepsilon''_{sL} - K^2 \varepsilon_{sL} = -K^2 \varepsilon_{hRL}, \tag{38}$$

where

$$K^2 = \frac{G_{bs}}{t_s E_s t_{bs}}. \tag{39}$$

Since the sensor has two stress-free ends, the boundary conditions can be constructed as

$$\begin{cases} \sigma_{sL}(x_1) = 0, \\ \sigma_{sL}(x_2) = 0, \end{cases} \tag{40}$$

where x_1, x_2 are the positions of the two ends of the sensor. By putting equation (37) into equation (40), the final solution to equation (38) yields

$$\varepsilon_{sL} = C_1 e^{Kx} + C_2 e^{-Kx} + \int_{x_1}^{x} -K\varepsilon_{hRL}(\theta) \times \sinh(K(x-\theta))\mathrm{d}\theta, \tag{41}$$

where

$$C_1 = \frac{\int_{x_1}^{x_2} K\varepsilon_{hRL}(\theta)\sinh(K(x_2-\theta))\mathrm{d}\theta}{e^{Kx_2} - e^{K(2x_1-x_2)}},$$

$$C_2 = -\frac{e^{2Kx_1}\int_{x_1}^{x_2} K\varepsilon_{hRL}(\theta)\sinh(K(x_2-\theta))\mathrm{d}\theta}{e^{Kx_2} - e^{K(2x_1-x_2)}}. \tag{42}$$

Once the normal strains of the sensor are obtained, the final linear voltage output of the sensor can be determined as [29]

$$V_{outL} = \frac{d_{31s} E_s t_s \int_{x_1}^{x_2} \varepsilon_{sL}\mathrm{d}x}{l_s (e_{33}{}^{\sigma} - d_{31s}{}^2 E_s)}, \tag{43}$$

where d_{31s}, l_s, and $e_{33}{}^{\sigma}$ are the piezoelectric constant, length and the dielectric constant of the sensor, respectively.

As the wave components related to the AAN are linearly captured by the sensor, we can follow the same process as the linear wave sensing problem. The corresponding nonlinear strain of the sensor can be determined with respect to the AAN-induced normal strain of the host structure as

$$\varepsilon_{sQ1} = C_3 e^{Kx} + C_4 e^{-Kx} + \int_{x_1}^{x} -K\varepsilon_{hRQ}(\theta) \times \sinh(K(x-\theta))\mathrm{d}\theta, \tag{44}$$

where

$$C_3 = \frac{\int_{x_1}^{x_2} K\varepsilon_{hRQ}(\theta)\sinh(K(x_2-\theta))\mathrm{d}\theta}{e^{Kx_2} - e^{K(2x_1-x_2)}},$$

$$C_4 = -\frac{e^{2Kx_1}\int_{x_1}^{x_2} K\varepsilon_{hRQ}(\theta)\sinh(K(x_2-\theta))\mathrm{d}\theta}{e^{Kx_2} - e^{K(2x_1-x_2)}}. \tag{45}$$

Thus, the voltage output corresponding to AAN will be calculated as V_{outQ1} according to equation (43).

Due to the material nonlinearity of the adhesive, an additional equivalent nonlinear normal stress, responsible for the SAN, is generated across the thickness of the bonding layer (shown in figure 3), written as

$$T_{bsQ} = -\frac{1}{4}(2B + A)\gamma_{bsL}{}^2, \tag{46}$$

where γ_{bsL} can be obtained by combining equation (35) and the constitutive equation of the bonding layer. As the SAN shares the same mechanism with AAN, the governing equations for the nonlinear wave sensing problem are identical to those in the nonlinear wave actuating process, with different subscripts used for the corresponding elements. Upon rearranging the terms, the differential equation with respect to τ_{sQ2} can be obtained

$$\tau''_{sQ2} - \Gamma_s{}^2 \tau_{sQ2} = \frac{G_{bs}\alpha}{E_h t_h t_{bs}} D(x) - \frac{1}{2} D''(x), \tag{47}$$

where

$$D(x) = -\frac{t_{bs}(2B + A)}{4}\frac{\mathrm{d}\gamma_{bsL}{}^2}{\mathrm{d}x}, \tag{48}$$

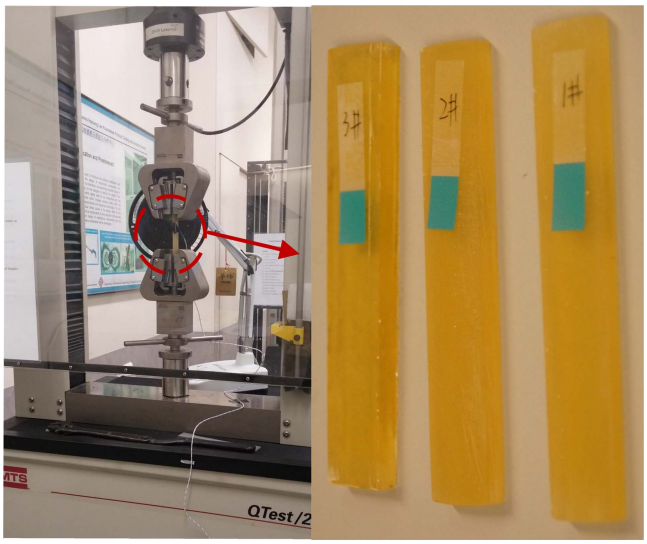

Figure 4. Experimental setup and specimens for measuring the elastic parameters of the adhesive.

$$\psi_s = \frac{t_h E_h}{t_s E_s}, \tag{49}$$

$$\Gamma_s^2 = \frac{G_{bs}}{t_{bs} t_s E_s} \frac{\alpha + \psi_s}{\psi_s}. \tag{50}$$

Similarly, the sensor and host structure have stress-free boundaries and the differential equation can be solved as

$$\tau_{sQ2} = C_5 e^{\Gamma_s x} + C_6 e^{-\Gamma_s x} + \int_{x_1}^{x} \frac{1}{\Gamma_s} \left(\frac{G_{bs}\alpha}{E_h t_h t_{bs}} D(\theta) - \frac{1}{2} D''(\theta) \right) \times \sinh(\Gamma_s(x-\theta)) \mathrm{d}\theta, \tag{51}$$

where

$$C_5 = \frac{M e^{\Gamma_s x_1} - N e^{\Gamma_s x_2} + e^{\Gamma_s x_2} \int_{x_1}^{x_2} \left(\frac{G_{bs}\alpha}{E_h t_h t_{bs}} D(\theta) - \frac{1}{2} D''(\theta) \right) \cosh(\Gamma_s(x_2-\theta)) \mathrm{d}\theta}{\Gamma_s (e^{2\Gamma_s x_1} - e^{2\Gamma_s x_2})},$$
$$C_6 = e^{2\Gamma_s x_1} \frac{M e^{\Gamma_s x_1} - N e^{\Gamma_s x_2} + e^{\Gamma_s x_2} \int_{x_1}^{x_2} \left(\frac{G_{bs}\alpha}{E_h t_h t_{bs}} D(\theta) - \frac{1}{2} D''(\theta) \right) \cosh(\Gamma_s(x_2-\theta)) \mathrm{d}\theta}{\Gamma_s (e^{2\Gamma_s x_1} - e^{2\Gamma_s x_2})} - \frac{M}{\Gamma_s} e^{\Gamma_s x_1} \tag{52}$$

and

$$M = \frac{t_{bs}(2B+A)}{8} \left. \frac{\mathrm{d}^2 {\gamma_{sL}}^2}{\mathrm{d}x^2} \right|_{x=x_1},$$
$$N = \frac{t_{bs}(2B+A)}{8} \left. \frac{\mathrm{d}^2 {\gamma_{sL}}^2}{\mathrm{d}x^2} \right|_{x=x_2}. \tag{53}$$

Detailed derivations can be found in appendix C. Once obtaining the shear stress distribution on the lower surface of the sensor, the normal strain related to the SAN can be further calculated according to the equilibrium equation of the sensor as

$$\varepsilon_{sQ2} = \int_{x_1}^{x} \frac{\tau_{sQ2}}{t_s E_s} \mathrm{d}x. \tag{54}$$

Finally, the corresponding voltage output will be obtained as V_{outQ1} according to equation (43).

The overall output voltage of the sensor is the superposition of the linear, ANN-induced and can SAN-induced signals, as

$$V_{out} = V_{outL} + V_{outQ1} + V_{outQ2}. \tag{55}$$

3. FE validations

FE method is first adopted to verify the theoretical model. The physical parameters of the adhesive which are used in both theoretical and FE models are obtained through experimental measurements. In the FE model, both AN and material nonlinearity of plate can be separately introduced to the relevant parts. Analysis focuses on four issues. First, the nonlinear feature extraction methods, crucial to the subsequent analyses, are highlighted and evaluated. Second, the theoretically predicted mechanism of the AN-induced nonlinear waves is validated, allowing a better understanding of the underlying phenomena. Third, the propagating characteristics of the AN-induced wave components are investigated, providing guidance for the following experimental characterization of the AN. Finally, the influence of the AN is assessed, justifying the practical need of considering AN effect in SHM applications.

3.1. Parameter justifications

The material parameters of the piezoelectric material [34] (PZT-C6 manufactured by Fuji Ceramics in the present case) and those of the aluminum [35] are readily available. However, the material parameters of the adhesive, especially its TOECs, are seldom provided in the existing literature. In this study, a tensile test was carried out to estimate the Young's modulus and TOECs of the adhesive.

Tensile tests were conducted with three samples made of UHU plus 2-component epoxy adhesive. The experiment was carried out at the room temperature with the tensile rate of 0.2 mm s^{-1}. The experimental set-up and the test specimens are illustrated in figure 4.

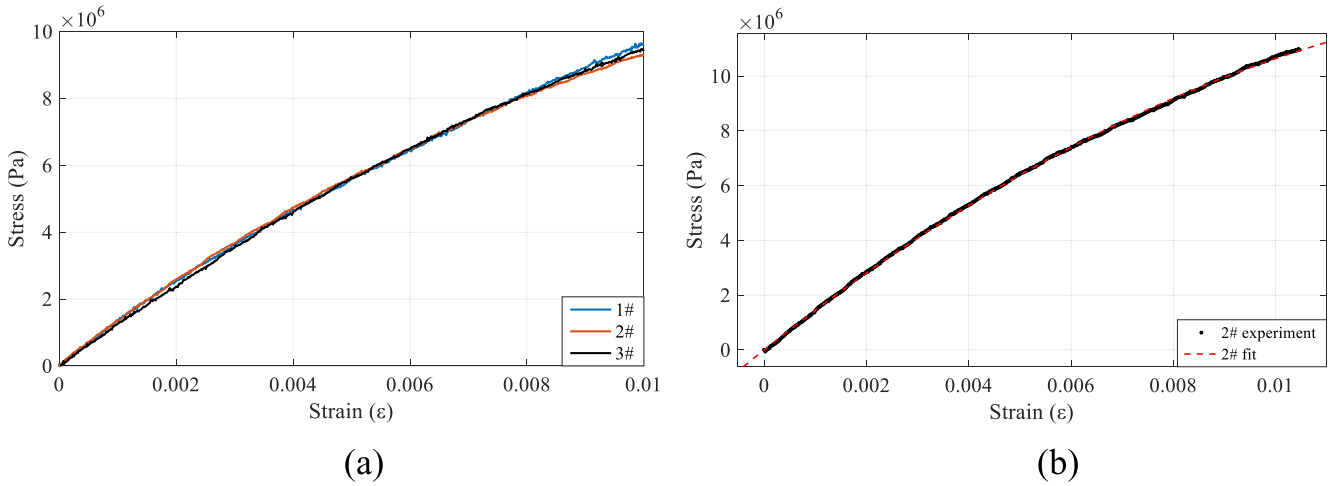

Figure 5. (a) Experimental results of the stress–strain curves of three samples. (b) Curve fitting results with the experimental result of specimen 2#.

Table 1. Proportional method to estimate the TOECs of adhesive.

	A	B	C	μ'
Aluminum	−702.4 Gpa	−280.8 Gpa	−205.6 Gpa	−1248 Gpa
Adhesive	−20.9 Gpa	−8.3 Gpa	−6.1 Gpa	−37.09 Gpa

Table 2. Parameters used in the theoretical and FE models.

PZT C6					
Width	Thickness	E	v	d_{31}	$e_{33}{}^{\sigma}$
8 mm	0.3 mm	62 Gpa	0.32	−210 pm V^{-1}	18.9 nF m^{-1}
Bonding layer					
Thickness	E	v[a]	A	B	C
0.03 mm	1.31 Gpa	0.4	−20.9 Gpa	−8.3 Gpa	−6.1 Gpa
Aluminum plate[b]					
Thickness	E	v	A	B	C
2 mm	69.56 Gpa	0.34	−702.4 Gpa	−280.8 Gpa	−205.6 Gpa

[a] The Poisson's ratio of the adhesive is assumed to be 0.4 which is the same as in [36].
[b] The TOECs of the aluminum are only used in the FE model to compare the influence of adhesive nonlinearity and that of material nonlinearity of the plate.

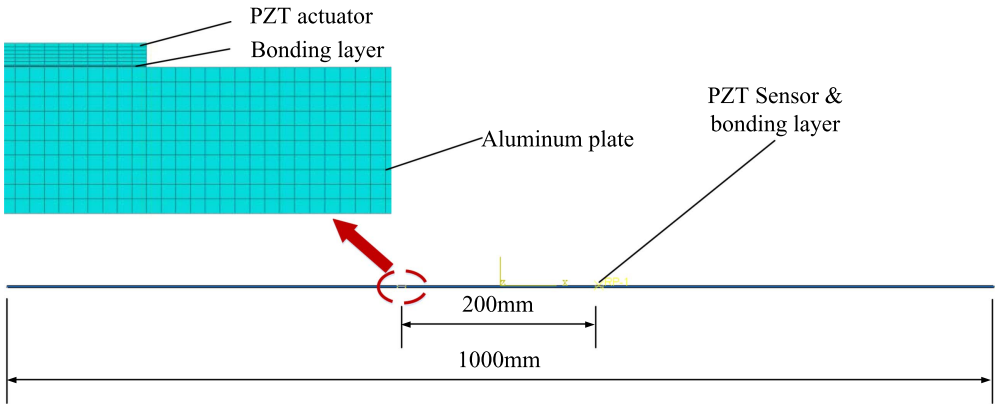

Figure 6. Sketch of the FE model.

The stress–strain curves from three tested specimens are shown in figure 5(a), which show fairly consistent results. Curve fitting was performed using the experimental results of sample 2# with a quadratic function, as

$$T = E\varepsilon + \mu'\varepsilon^2. \tag{56}$$

The fitted curve shown in figure 5(b) gives the parameters in terms of the Young's modulus ($E = 1.310$ GPa) and the nonlinear elastic parameter ($\mu' = -37.09$ GPa). In order to estimate the TOECs of the adhesive, a proportion method is adopted here. The μ' of the aluminum can be firstly calculated with its TOECs by comparing equations (3) and (56). Then, we calculate the ratio between experimentally obtained μ' of the adhesive and theoretical μ' of the aluminum. Finally, the TOECs of the adhesive can be determined by the calculated ratio, with results tabulated in table 1. In addition, all the parameters used in the FE model and theoretical model are listed in table 2.

3.2. FE model description

A 2D FE model is established using ABAQUS, as sketched in figure 6. Two identical piezoelectric transducers, used as actuator and sensor respectively, are glued to an aluminum plate. For simplicity, their corresponding bonding layers are also assumed to have the same dimensions and material properties. Tie constraints are applied to model the interactions between individual parts, thus assuring the displacement continuity between the pairs of tied surfaces. Plane strain elements are attributed to all the parts with fine meshes whose size is smaller than 10% of the shortest wavelength of interest. In order to strike a balance between the signal complexity resulting from the boundary reflections and the calculation cost, the total length of the plate is set to 1000 mm and the distance between the actuator and the sensor is 200 mm. GN can either be included or excluded so that its influence can be evaluated. In this model, the piezoelectric material is assumed to have linear elastic and electric properties while the adhesive and the plate can be linear or nonlinear in elasticity as needed. The nonlinear material behavior is programmed with the ABAQUS UMAT user subroutine according to the Landau–Lifshitz model. As a typical example, the excitation for both the theoretical and FE models is chosen as a 5-cycle tone-burst signal with an amplitude of 160 V and a center frequency of 60 kHz. In this case, only S_0 and A_0 mode Lamb waves can be generated in the plate based on their dispersion curves (not shown here).

3.3. Nonlinear feature extraction

In order to validate the theoretical model, the nonlinear features in the FE results need to be extracted. Two possible methods can potentially be used. The first one is the baseline method, in which the baseline signal needs to be obtained in advance in the absence of any nonlinear sources in the system. The nonlinear features can then be extracted by subtracting the baseline signal from the overall system response signal. Though accurate in principle, the method is not feasible to use in practice since the purely linear baseline can hardly be obtained. The second method is referred to as the superposition method, originally reported by Kim [37]. The second harmonic nonlinear part is extracted by superposing two response signals resulting from the excitations which are opposite in phase. Through this method, the linear and odd harmonic components are eliminated in principle. In addition, the method allows obtaining the nonlinear response in time domain which includes amplitude, temporal and phase information. In the present case, an evaluation is carried out to demonstrate its validity for the nonlinear feature extraction, which was lacking in the original work of Kim.

As a comparison, results from FE simulation are treated by the baseline method and the superposition method, respectively, with results being plotted together in figure 7(a) to validate the superposition method. Noticeable differences between the two methods can be observed. By carrying out the FFT to the windowed signals, it becomes clear that the observed differences are due to the presence of the linear and the odd harmonic responses, which is consistent with the above analyses (shown in figure 7(b)). This suggests that the superposition method is feasible to extract all the even harmonic nonlinear responses. Moreover, it is able to preserve their amplitude, temporal and phase information. These features make the superposition method attractive for real applications.

3.4. Demonstration of the mechanism of AN

The established theoretical model reveals that the AAN-induced second harmonic response results from an equivalent nonlinear normal stress exerting over the thickness-through cross section of the bonding layer and its induced second harmonic normal strain. To verify this theoretically predicted mechanism, the averaged nonlinear normal strain of one element in the bonding layer is extracted using the superposition method, as shown in figure 8. It can be seen that the nonlinear response mainly contains the 120 kHz wave component, which demonstrates the second-harmonic normal strain is indeed generated in the bonding layer. Through its coupling with the host structure, the second-harmonic Lamb waves is further generated in the host structure, which is consistent with the theoretical prediction.

Furthermore, the linear, AAN-induced and SAN-induced voltage responses, predicted by the model, are also compared with the FE results in figure 9. The agreement between the theoretical results and FE ones in terms of both temporal and phase is obvious in both linear and nonlinear responses despite some noticeable differences in the signal amplitude. This difference may be attributed to the assumptions used in the theoretical model like the 1D assumption, omission of the inertial terms, ignorance of the influence of the sensor on the propagating waves and so on. Same as the linear model [31], the model developed here is not intended to reproduce every single detail of the signal, especially in terms of amplitude, but to reveal the higher-order wave generation mechanism

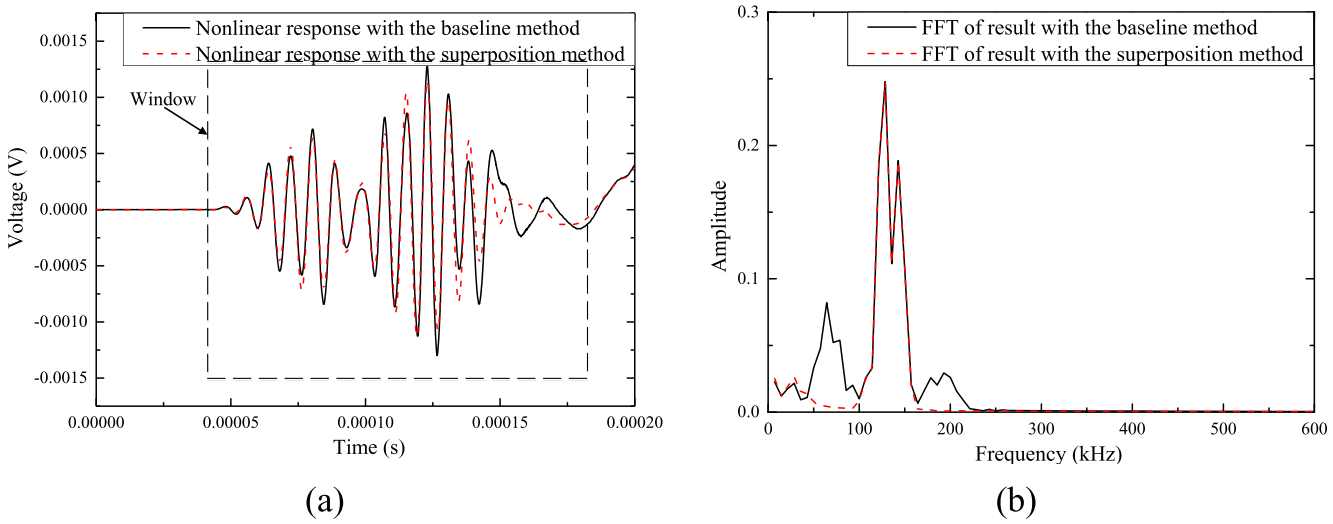

Figure 7. (a) Comparison of the nonlinear responses obtained with baseline method and superposition method and (b) the FFT results of the nonlinear responses.

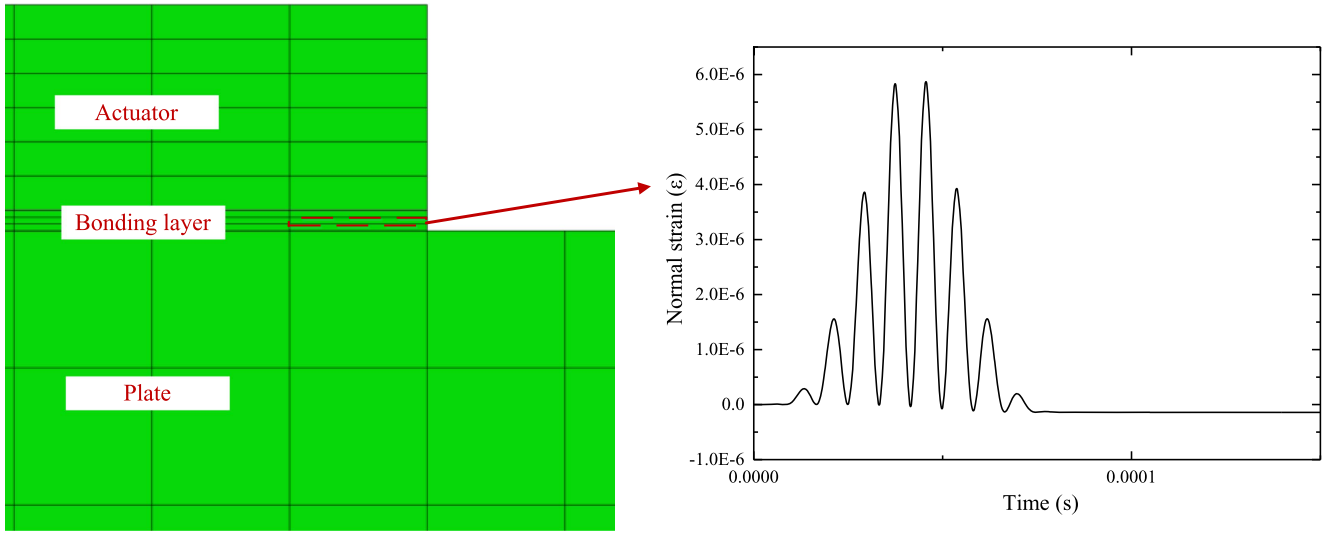

Figure 8. Nonlinear normal strain at the edge of the bonding layer at the actuator-plate interaction.

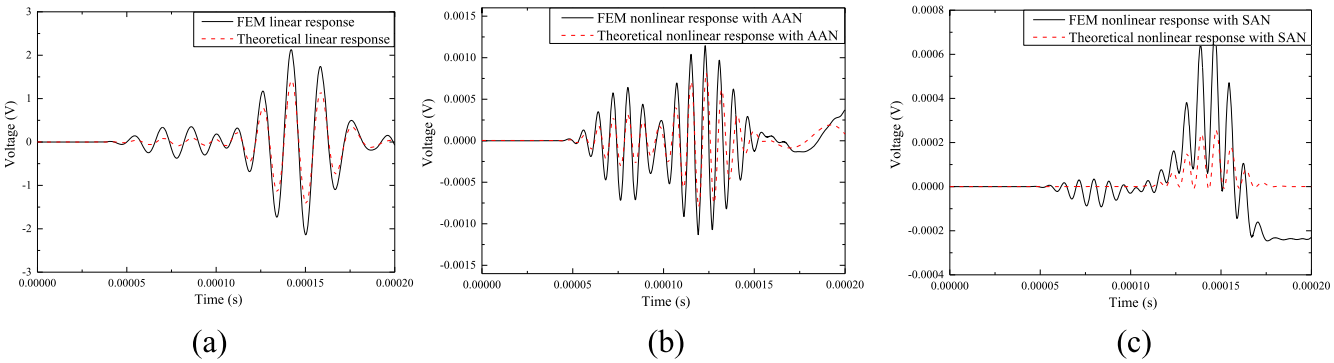

Figure 9. Comparison of the linear and nonlinear results between the theoretical and FE models: (a) linear responses with 60 kHz excitation; (b) AAN-induced responses with 60 kHz excitation; (c) SAN-induced responses with 60 kHz excitation.

and characteristics of AN. In that perspective, the agreement between the two sets of results is deemed acceptable, able to validate the model as well as the AN-related wave generation mechanism of AN from the model. The temporal and phase information will be further utilized to investigate the propagating characteristics of the AN-induced wave components.

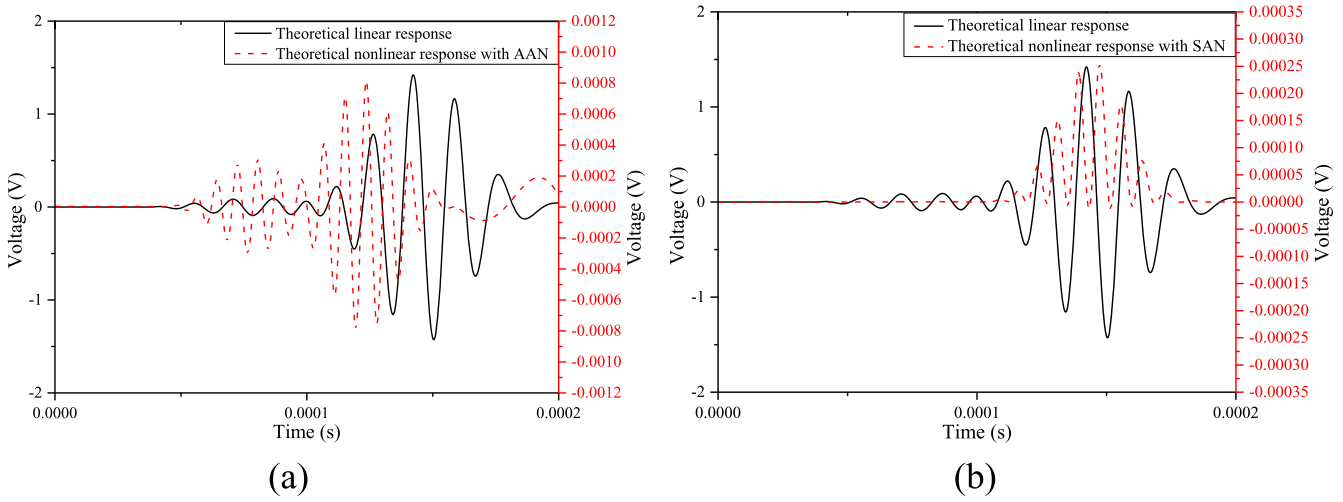

Figure 10. (a) Theoretical linear and AAN-induced responses with 60 kHz excitation; (b) theoretical linear and SAN-induced responses with 60 kHz excitation.

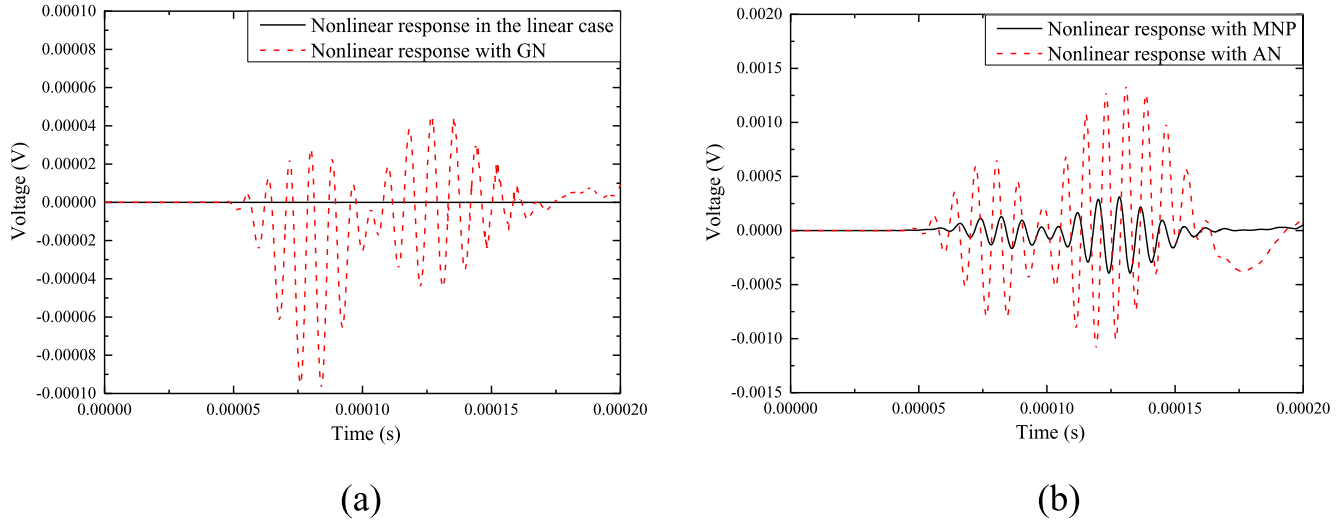

Figure 11. Comparison of nonlinear responses in the (a) linear case and nonlinear case with geometric nonlinearity; (b) nonlinear case with AN and MNP when the exciting frequency is 60 kHz.

3.5. Propagating characteristics of AN-induced wave components

Upon obtaining the linear, AAN-induced and SAN-induced responses, the propagating characteristics of the AN-induced wave components can be investigated according to the temporal and phase information of the responses. Owing to their agreement with the FE results, only results from the established model, shown in figure 10, are used in this section. As the group velocity of the A_0 mode Lamb waves at 120 kHz is different from, and much higher than that at 60 kHz, figure 10(a) shows that the AAN-induced wave components propagate independently at their respective velocities, as evidenced by the difference in their respective arrival time. In contrast, the SAN-induced waves is captured simultaneously with the linear wave component, as shown in figure 10(b). The difference between the propagating characteristics of the AAN-induced and SAN-induced wave components can provide guidance for the further identification of these two nonlinear sources in the experiments.

3.6. Evaluation of the influence of AN

As both AN and material nonlinearity can be separately introduced to the FE model, the influence of the AN can be quantitatively evaluated. Four cases are considered in the FE simulations: with only linear properties, only GN, material nonlinearity of the plate (MNP) and AN containing both AAN and SAN in the system. The effect of the GN is included in the MNP and AN cases. The nonlinear responses with different nonlinear sources are shown in figure 11. The pure linear case is shown in figure 11(a), exhibiting no nonlinear feature in the signal as expected. When GN, MNP or AN is introduced to the system, the nonlinear responses can

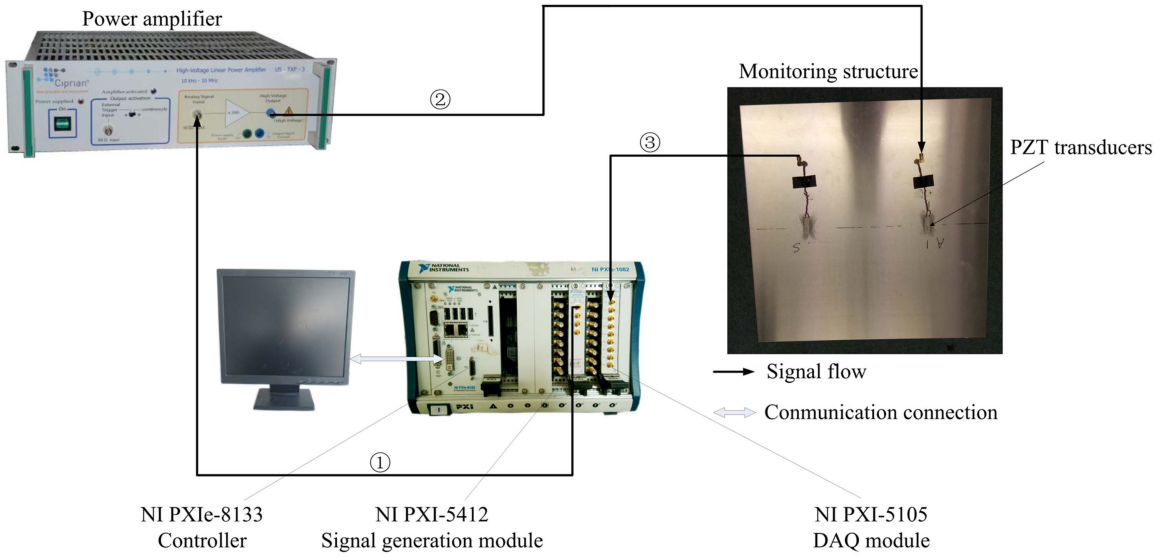

Figure 12. Experimental set-up.

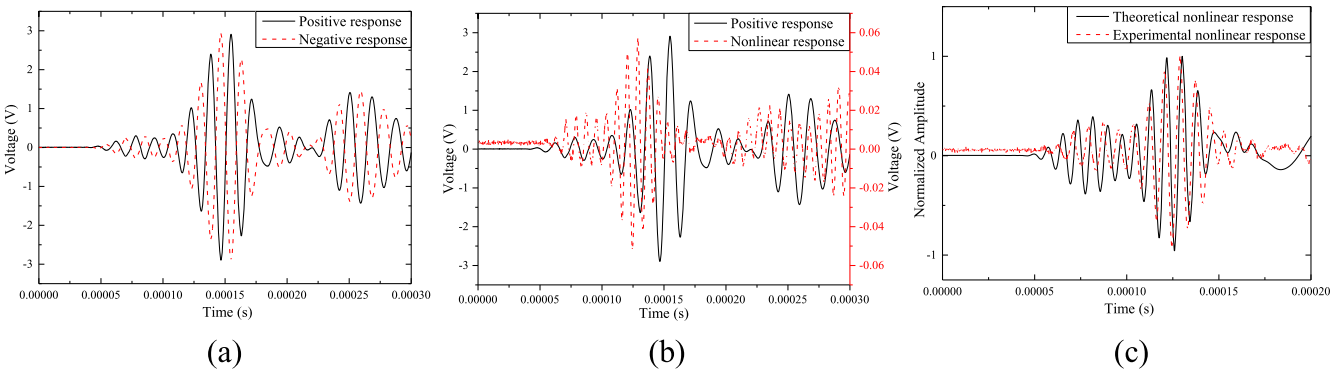

Figure 13. (a) Responses to the opposed excitations at 60 kHz; (b) response to the positive excitation at 60 kHz and extracted nonlinear responses with the superposition method; (c) the normalized theoretical and experimental nonlinear responses.

be captured through the superposition method. Compared with that of the MNP and the AN, the influence of the GN is indeed negligible, as reflected by its small amplitude of nonlinear response (figure 11(a)). In addition, the amplitude of the nonlinear response in the case of the AN is much larger than that of the MNP. It can be concluded from the above analyses that, AN is a non-negligible nonlinear source in a typical nonlinear Lamb-wave-based SHM system. Without its proper consideration, conventional nonlinear acousto-guided wave based SHM methods could be compromised.

4. Experimental validations

Experiments were carried out to further validate the model mainly in terms of the frequency tuning characteristics of AN-induced waves. In the following, the basic characteristics of the nonlinear response in the experiment are first discussed. After that, the frequency tuning curves from the theoretical model and the experiments are compared to validate the model.

4.1. Experimental setup

The experimental set-up is illustrated in figure 12. Two rectangular piezoelectric transducers (30 mm*8 mm*0.3 mm) were bonded on an aluminum plate (400 mm*400 mm*2 mm) with the epoxy adhesive tested in section 3.1. The distance between the two transducers was 200 mm and the thickness of the bonding layer was approximately 30 μm which was measured by Mitutoyo's micrometer. The whole system works as follow: the controller commands the NI-PXI5412 signal generation module to output a tone burst exciting signal. The low-voltage signal then passes through the Ciprian US-TXP-3 power amplifier and the amplified output is applied to the piezoelectric transducer to generate Lamb waves in the plate. Responses of Lamb waves are then acquired by the NI-PXI5105 data acquisition module, stored and processed by the controller.

4.2. Analysis of the nonlinear response

In the experiment, a pair of five-cycle tone burst signals at the central frequency of 60 kHz with reversed phase were

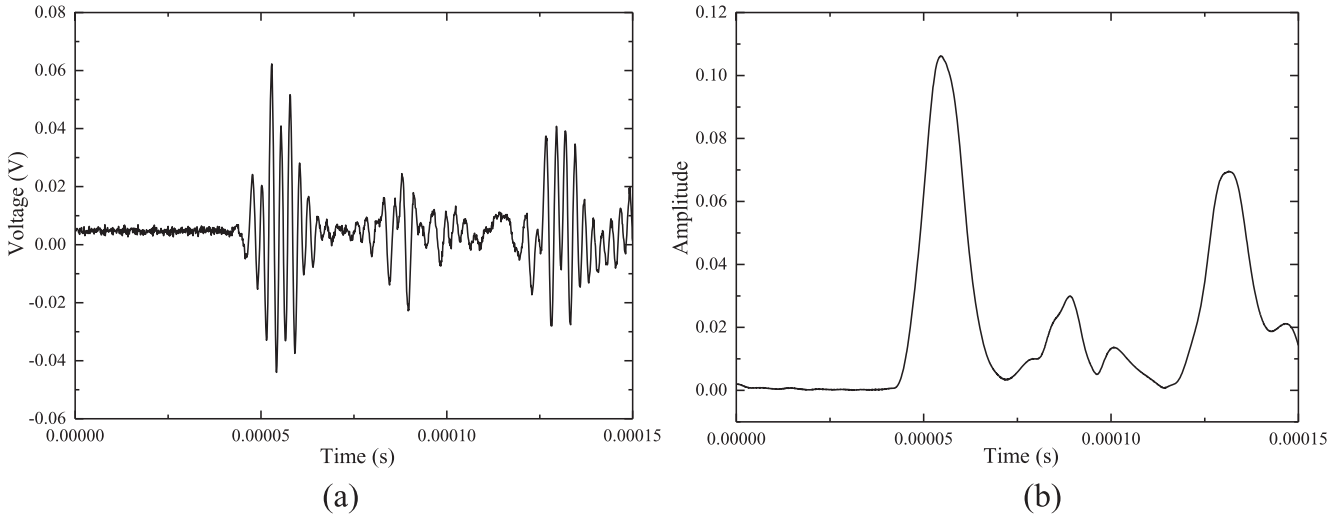

Figure 14. (a) Nonlinear responses extracted by the superposition method with an excitation at 200 kHz; (b) the modulus of the wavelet coefficients at 400 kHz.

separately used as the excitation of Lamb waves. Setting the amplitude of the excitation to 160 V, the responses to the pair of excitations are shown in figure 13(a). The superposition method was used again, allowing obtaining the corresponding nonlinear response which is about 2% in the amplitude of the primary wave components in amplitude, as shown in figure 13(b). As the instruments have low nonlinearity according to the manufacturers [38–40] and the influence of the material nonlinearity of the plate in this specific configuration is weak, as evidenced by the previous FE results, it is believed that the captured nonlinear response is mainly associated with AN.

The normalized nonlinear response is compared with the theoretical one which combines both AAN and SAN effects, as illustrated in figure 13(c). The agreement between the two sets of results demonstrates again the propagating characteristics of the AN-induced nonlinear wave components. In light of the propagating characterizes analyzed before, the SAN-generated nonlinear A_0 mode wave should only appear at the time when primary A_0 mode wave reaches the sensing position. It can be seen from figure 13(b), however, that part of the nonlinear signal is weak, thus suggesting the weak nonlinearity induced by SAN, in agreement with the theoretical results predicted by the established model (figure 10(a) and figure 10 (b)). The plausible explanation is that, while all the input energy passes through the actuator-plate interface, only part of it flows across the sensor-plate bonding layer so that adhesive over the sensor-plate interface undergoes smaller deformation as its counterparts at actuation does.

4.3. Frequency tuning characteristics of the nonlinear wave components

Guided by the previous linear work [31], the nonlinear frequency tuning characteristics of the system are experimentally investigated to further validate the theoretical model. The focus is put on the S_0 mode Lamb waves since they show the promising cumulative effect on one hand and can be easily identified from the temporal responses as the first arrival wave package on the other hand, both being conducive to SHM applications. In the experiments, the excitation frequency range was chosen from 60 to 300 kHz. Take 200 kHz excitation as an example, the acquired sensor signal is first treated using superposition method, giving nonlinear response signal depicted in figure 14(a). The complex Morlet wavelet transform is then applied to extract the amplitude of the signal. Detailed signal processing procedure can be found in our previous work [6]. Results in terms of the modulus of the wavelet coefficients at 400 kHz are shown in figure 14(b), from which we can precisely obtain the amplitude value of the nonlinear second-harmonic S_0 mode responses. The same wavelet transform is also applied to the nonlinear responses from the theoretical model to keep the consistency of the analysis. This results in the normalized frequency tuning curves of the nonlinear S_0 mode Lamb waves, plotted in figure 15. It can be seen that both sets of results show a very

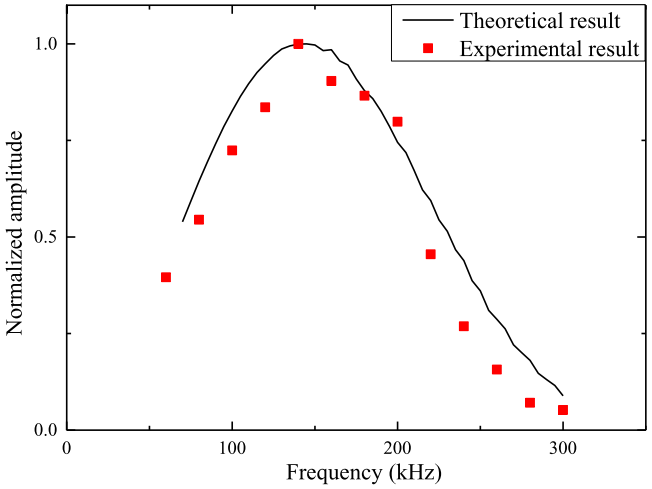

Figure 15. Normalized frequency tuning curves of the nonlinear S_0 mode Lamb waves obtained in the theoretical model and the experiments.

similar tendency, which again validates the frequency tuning characteristics revealed by the theoretical model. For further application, the frequency tuning characteristics can be exploited and utilized for optimizing the system configuration to minimize the adverse influence of AN in an SHM system.

5. Conclusions

In this paper, a nonlinear theoretical framework is proposed to investigate the mechanism and characteristics of the AN and its effect on a typical PZT-actuated and nonlinear Lamb-wave-based structural health monitoring system. The proposed model combines the entire processes of Lamb wave generation, propagation and sensing, allowing the assessment of the contributions of various physical components involved. The model incorporates both linear and nonlinear contributions from various parts of the system which can be solved through the perturbation method. The reduced linear problem retreats to the classical shear-lag solutions as a special case. The nonlinear problem is formulated to show the existence of an equivalent nonlinear normal stress in the bonding layer, originated from the nonlinear material behavior and responsible for the generation of non-negligible second harmonic responses in the captured sensor signals. The model is validated with both FE and experimental results in various aspects which are relevant to SHM applications. The mechanism as well as the propagating characteristics of AN-induced Lamb waves is confirmed through comparisons with FE results. Meanwhile, the influences of AN and MNP are separated, quantified and compared. The frequency tuning characteristics of AN-induced S_0 mode Lamb waves are also validated through experiments. In particular, a superposition method is applied to extract the nonlinear feature from the overall system responses.

Results demonstrate the non-negligible nonlinear effects of the bonding layers in a typical PZT-actuated SHM system. The AAN-induced Lamb waves propagate independently of the primary Lamb wave modes in the structure while the SAN-induced wave components are captured simultaneously with the primary Lamb waves. In addition, the agreement of the frequency tuning characteristics of S_0 mode nonlinear Lamb waves from the theoretical and experimental results proves the validity of the theoretical framework. Furthermore, both the theoretical model and the experimental results indicate that AAN acts as a much stronger nonlinear source with appreciable influence on the nonlinear SHM system when compared with the SAN.

The above findings suggest the necessity of considering the adhesive as one of the non-negligible nonlinear contributors in information processing and SHM system design in general. In that regard, the proposed theoretical model will definitely be useful in performing system analysis, design and eventually optimization to minimize the effect of the AN in SHM systems. As the influence of AAN is shown to be dominant in the AN-induced nonlinear response, the main focus of the further optimization should be on the actuator configuration.

Acknowledgments

The authors wish to acknowledge a grant from Research Grants Council of Hong Kong Special Administrative Region (PolyU 152070/16E).

Appendix A. Nonlinear material behavior under uniaxial tension and pure shearing

The Landau–Lifshitz stress–strain relation can be written in the form of individual components as:

$$\begin{aligned} T_1 = {} & \lambda(\varepsilon_1+\varepsilon_2+\varepsilon_3) + 2\mu\varepsilon_1 + C(\varepsilon_1+\varepsilon_2+\varepsilon_3)^2 \\ & + B(\varepsilon_1^2+\varepsilon_2^2+\varepsilon_3^2+2\varepsilon_{12}^2+2\varepsilon_{13}^2+2\varepsilon_{23}^2) \\ & + 2B(\varepsilon_1+\varepsilon_2+\varepsilon_3)\varepsilon_1 + A(\varepsilon_1^2+\varepsilon_{12}^2+\varepsilon_{13}^2), \end{aligned} \tag{A.1}$$

$$\begin{aligned} T_2 = {} & \lambda(\varepsilon_1+\varepsilon_2+\varepsilon_3) + 2\mu\varepsilon_2 + C(\varepsilon_1+\varepsilon_2+\varepsilon_3)^2 \\ & + B(\varepsilon_1^2+\varepsilon_2^2+\varepsilon_3^2+2\varepsilon_{12}^2+2\varepsilon_{13}^2+2\varepsilon_{23}^2) \\ & + 2B(\varepsilon_1+\varepsilon_2+\varepsilon_3)\varepsilon_2 + A(\varepsilon_2^2+\varepsilon_{12}^2+\varepsilon_{23}^2), \end{aligned} \tag{A.2}$$

$$\begin{aligned} T_3 = {} & \lambda(\varepsilon_1+\varepsilon_2+\varepsilon_3) + 2\mu\varepsilon_3 + C(\varepsilon_1+\varepsilon_2+\varepsilon_3)^2 \\ & + B(\varepsilon_1^2+\varepsilon_2^2+\varepsilon_3^2+2\varepsilon_{12}^2+2\varepsilon_{13}^2+2\varepsilon_{23}^2) \\ & + 2B(\varepsilon_1+\varepsilon_2+\varepsilon_3)\varepsilon_3 + A(\varepsilon_3^2+\varepsilon_{32}^2+\varepsilon_{13}^2), \end{aligned} \tag{A.3}$$

$$\begin{aligned} T_{12} = {} & 2\mu\varepsilon_{12} + 2B(\varepsilon_1+\varepsilon_2+\varepsilon_3)\varepsilon_{12} \\ & + A(\varepsilon_1\varepsilon_{12}+\varepsilon_2\varepsilon_{12}+\varepsilon_{31}\varepsilon_{32}), \end{aligned} \tag{A.4}$$

$$\begin{aligned} T_{13} = {} & 2\mu\varepsilon_{13} + 2B(\varepsilon_1+\varepsilon_2+\varepsilon_3)\varepsilon_{13} \\ & + A(\varepsilon_1\varepsilon_{13}+\varepsilon_3\varepsilon_{31}+\varepsilon_{32}\varepsilon_{21}), \end{aligned} \tag{A.5}$$

$$\begin{aligned} T_{23} = {} & 2\mu\varepsilon_{23} + 2B(\varepsilon_1+\varepsilon_2+\varepsilon_3)\varepsilon_{23} \\ & + A(\varepsilon_{23}\varepsilon_3+\varepsilon_2\varepsilon_{23}+\varepsilon_{13}\varepsilon_{21}). \end{aligned} \tag{A.6}$$

During the uniaxial tensile process in the x_1 direction, the normal strains in the three directions are expected to have the same order of magnitude. The shear stresses and strains should be equal to zero. Meanwhile, the normal stresses in the x_2, x_3 direction are also equal to zero. The stress-strain relation can be reduced to

$$\begin{aligned} T_1 = {} & \lambda(\varepsilon_1+\varepsilon_2+\varepsilon_3) + 2\mu\varepsilon_1 + C(\varepsilon_1+\varepsilon_2+\varepsilon_3)^2 \\ & + B(\varepsilon_1^2+\varepsilon_2^2+\varepsilon_3^2) + 2B(\varepsilon_1+\varepsilon_2+\varepsilon_3)\varepsilon_1 + A\varepsilon_1^2, \end{aligned} \tag{A.7}$$

$$\begin{aligned} 0 = {} & \lambda(\varepsilon_1+\varepsilon_2+\varepsilon_3) + 2\mu\varepsilon_2 + C(\varepsilon_1+\varepsilon_2+\varepsilon_3)^2 \\ & + B(\varepsilon_1^2+\varepsilon_2^2+\varepsilon_3^2) + 2B(\varepsilon_1+\varepsilon_2+\varepsilon_3)\varepsilon_2 + A\varepsilon_2^2, \end{aligned} \tag{A.8}$$

$$\begin{aligned} 0 = {} & \lambda(\varepsilon_1+\varepsilon_2+\varepsilon_3) + 2\mu\varepsilon_3 + C(\varepsilon_1+\varepsilon_2+\varepsilon_3)^2 \\ & + B(\varepsilon_1^2+\varepsilon_2^2+\varepsilon_3^2) + 2B(\varepsilon_1+\varepsilon_2+\varepsilon_3)\varepsilon_3 + A\varepsilon_3^2. \end{aligned} \tag{A.9}$$

Putting equations (A.8) and (A.9) into equation (A.7), the nonlinear stress–strain relationship in uniaxial tension can be obtained:

$$T_1 = E\varepsilon_1 + \left[C\left(\frac{\mu}{\lambda+\mu}\right)^2 + B\left(1 + 2\left(\frac{\lambda}{2(\lambda+\mu)}\right)^2\right) + 2B\left(\frac{\mu}{\lambda+\mu}\right) + A\right]\varepsilon_1{}^2, \tag{A.10}$$

where E is the Young's modulus which is related to the Lamé constants as $E = \mu(3\lambda + 2\mu)/(\lambda + \mu)$.

Under pure shearing in x_1–x_2 plane, the shear stresses and strains in the x_1–x_3 plane and x_2–x_3 plane are equal to zero. Meanwhile, the normal stresses are also zero. The stress–strain relations write

$$0 = \lambda(\varepsilon_1 + \varepsilon_2 + \varepsilon_3) + 2\mu\varepsilon_1 + C(\varepsilon_1 + \varepsilon_2 + \varepsilon_3)^2 + B(\varepsilon_1{}^2 + \varepsilon_2{}^2 + \varepsilon_3{}^2 + 2\varepsilon_{12}{}^2) + 2B(\varepsilon_1 + \varepsilon_2 + \varepsilon_3)\varepsilon_1 + A(\varepsilon_1{}^2 + \varepsilon_{12}{}^2), \tag{A.11}$$

$$0 = \lambda(\varepsilon_1 + \varepsilon_2 + \varepsilon_3) + 2\mu\varepsilon_2 + C(\varepsilon_1 + \varepsilon_2 + \varepsilon_3)^2 + B(\varepsilon_1{}^2 + \varepsilon_2{}^2 + \varepsilon_3{}^2 + 2\varepsilon_{12}{}^2) + 2B(\varepsilon_1 + \varepsilon_2 + \varepsilon_3)\varepsilon_2 + A(\varepsilon_2{}^2 + \varepsilon_{12}{}^2), \tag{A.12}$$

$$0 = \lambda(\varepsilon_1 + \varepsilon_2 + \varepsilon_3) + 2\mu\varepsilon_3 + C(\varepsilon_1 + \varepsilon_2 + \varepsilon_3)^2 + B(\varepsilon_1{}^2 + \varepsilon_2{}^2 + \varepsilon_3{}^2 + 2\varepsilon_{12}{}^2) + 2B(\varepsilon_1 + \varepsilon_2 + \varepsilon_3)\varepsilon_3 + A\varepsilon_3{}^2, \tag{A.13}$$

$$T_{12} = 2\mu\varepsilon_{12} + 2B(\varepsilon_1 + \varepsilon_2 + \varepsilon_3)\varepsilon_{12} + A(\varepsilon_1\varepsilon_{12} + \varepsilon_2\varepsilon_{12}). \tag{A.14}$$

As the shear strain is a small value under the small deformation assumption, the normal strains are in the same order of the magnitude of $\varepsilon_{12}{}^2$ from equations (A.11)–(A.13). In this case, the normal strains become negligible compared to ε_{12}. Any terms in equations from (A.11) to (A.13) with the order of magnitude higher than $\varepsilon_{12}{}^3$ can be eliminated. The stress–strain relation can be further reduced to

$$0 = \lambda(\varepsilon_1 + \varepsilon_2 + \varepsilon_3) + 2\mu\varepsilon_1 + (2B + A)\varepsilon_{12}{}^2, \tag{A.15}$$

$$0 = \lambda(\varepsilon_1 + \varepsilon_2 + \varepsilon_3) + 2\mu\varepsilon_2 + (2B + A)\varepsilon_{12}{}^2, \tag{A.16}$$

$$0 = \lambda(\varepsilon_1 + \varepsilon_2 + \varepsilon_3) + 2\mu\varepsilon_3 + 2B\varepsilon_{12}{}^2, \tag{A.17}$$

$$T_{12} = 2\mu\varepsilon_{12} + 2B(\varepsilon_1 + \varepsilon_2 + \varepsilon_3)\varepsilon_{12} + A(\varepsilon_1\varepsilon_{12} + \varepsilon_2\varepsilon_{12}). \tag{A.18}$$

By substituting equations (A.15)–(A.17) into equation (A.18), the nonlinear shear–stress–strain relation can be obtained as

$$T_{12} = 2\mu\varepsilon_{12} + \left[2A\left(\frac{\lambda(3B + A)}{\mu(3\lambda + 2\mu)} - \frac{2B + A}{2\mu}\right) - 2B\left(\frac{6B + 2A}{3\lambda + 2\mu}\right)\right]\varepsilon_{12}{}^3. \tag{A.19}$$

Appendix B. Nonlinear shear-lag solution for wave generation

The governing equations for the nonlinear shear-lag model are summarized as follows in terms of the constitutive equations from (B.1) to (B.3), geometric equations from (B.4) to (B.6) and equilibrium equations from (B.7) to (B.10),

$$\sigma_{aQ} = E_a\varepsilon_{aQ}, \tag{B.1}$$

$$\tau_{baQ} = G_{ba}\gamma_{baQ}, \tag{B.2}$$

$$\sigma_{hQ} = E_h\varepsilon_{hQ}, \tag{B.3}$$

$$\varepsilon_{aQ} = \frac{du_{aQ}}{dx}, \tag{B.4}$$

$$\gamma_{baQ} = \frac{u_{aQ} - u_{hQ}}{t_{ba}}, \tag{B.5}$$

$$\varepsilon_{hQ} = \frac{du_{hQ}}{dx}, \tag{B.6}$$

$$t_aE_a\varepsilon'_{aQ} - \tau_{aQ} = 0, \tag{B.7}$$

$$t_{ba}\frac{dT_{baQ}}{dx} + \tau_{aQ} - \tau_{hQ} = 0, \tag{B.8}$$

$$\frac{\tau_{aQ} + \tau_{hQ}}{2} = \tau_{baQ}, \tag{B.9}$$

$$t_hE_h\varepsilon'_{hQ} + \alpha\tau_{hQ} = 0. \tag{B.10}$$

Putting equation (22) into equation (B.8) yields

$$\tau_{aQ} = \tau_{hQ} + \frac{(2B + A)\varepsilon_{ISA}{}^2}{4t_{ba}\Gamma_a(\cosh(\Gamma_a a))^2}\sinh(2\Gamma_a x) = \tau_{hQ} + P\sinh(2\Gamma_a x). \tag{B.11}$$

By using the equation resulted from equation (B.7) multiplied by t_hE_h to subtract the equation resulted from equation (B.10) multiplied by t_aE_a and substituting equation (B.11) into the resulted equation, one gets

$$t_aE_at_hE_h(\varepsilon'_{aQ} - \varepsilon'_{hQ}) = (t_hE_h + \alpha t_aE_a)\tau_{hQ} + t_hE_hC\sinh(2\Gamma_a x). \tag{B.12}$$

After putting equations (B.4)–(B.6) and (B.2) into equation (B.12), one has

$$\tau''_{baQ} = \frac{G_{ba}(t_hE_h + \alpha t_aE_a)}{t_{ba}t_at_hE_aE_h}\tau_{hQ} + \frac{P}{t_{ba}t_aE_a}\sinh(2\Gamma_a x) \tag{B.13}$$

By further putting equation (B.11) into equation (B.9) and then substituting the result into equation (B.13), the differential equation with the notions of equations (20) and (21) is obtained as follows:

$$\tau''_{hQ} - \Gamma_a^2\tau_{hQ} = P\left(\frac{G_{ba}}{t_{ba}t_aE_a} - 2\Gamma_a{}^2\right)\times\sinh(2\Gamma_a x) = R\sinh(2\Gamma_a x). \tag{B.14}$$

The stress-free boundary conditions are given as

$$\begin{cases}\sigma_{aQ}(\pm a) = 0,\\ \sigma_{hQ}(\pm a) = 0.\end{cases} \tag{B.15}$$

Putting equation (B.1) into equation (B.6) and then into equation (B.9) and finally into equation (B.15) leads to the following equation:

$$\frac{\tau'_{aQ}(\pm a) + \tau'_{hQ}(\pm a)}{2} = \frac{G_{ba}}{t_{ba}}(u'_{aQ}(\pm a) - u'_{hQ}(\pm a)) = 0. \quad \text{(B.16)}$$

Then, putting equation (B.11) into equation (B.16) yields

$$\tau'_{hQ}(\pm a) = -P\Gamma_a \cosh(2\Gamma_a a). \quad \text{(B.17)}$$

Combining equation (B.14) and (B.16) leads to the final solution, expressed as

$$\tau_{hQ} = -\left(\frac{2R}{3\Gamma_a{}^2} + P\right)\frac{\cosh(2\Gamma_a a)}{\cosh(\Gamma_a a)}\sinh(\Gamma_a x) + \frac{R}{3\Gamma_a{}^2}\sinh(2\Gamma_a x). \quad \text{(B.18)}$$

Appendix C. Wave sensing of SAN-induced wave components

The governing equations for the nonlinear wave sensing problem are summarized as follows in terms of the constitutive equations from equations (C.1) to (C.3), geometric equations from equations (C.4) to (C.6) and equilibrium equations from equations (C.7) to (C.10),

$$\sigma_{sQ2} = E_s\varepsilon_{sQ2}, \quad \text{(C.1)}$$

$$\tau_{bsQ2} = G_{bs}\gamma_{bsQ2}, \quad \text{(C.2)}$$

$$\sigma_{hQ2} = E_h\varepsilon_{hQ2}, \quad \text{(C.3)}$$

$$\varepsilon_{sQ2} = \frac{du_{sQ2}}{dx}, \quad \text{(C.4)}$$

$$\gamma_{bsQ2} = \frac{u_{sQ2} - u_{hQ2}}{t_{bs}}, \quad \text{(C.5)}$$

$$\varepsilon_{hQ2} = \frac{du_{hQ2}}{dx}, \quad \text{(C.6)}$$

$$t_s E_s \varepsilon'_{sQ2} - \tau_{sQ2} = 0, \quad \text{(C.7)}$$

$$t_{bs}\frac{dT_{bsQ}}{dx} + \tau_{sQ2} - \tau_{hQ2} = 0, \quad \text{(C.8)}$$

$$\frac{\tau_{sQ2} + \tau_{hQ2}}{2} = \tau_{bsQ2}, \quad \text{(C.9)}$$

$$t_h E_h \varepsilon'_{hQ2} + \alpha\tau_{hQ2} = 0. \quad \text{(C.10)}$$

Putting equation (46) into equation (C.8) gives

$$\tau_{hQ2} = \tau_{sQ2} - \frac{t_{bs}(2B + A)}{4}\frac{d\gamma_{bsL}{}^2}{dx} = \tau_{sQ2} + D(x). \quad \text{(C.11)}$$

Following the same process as detailed in appendix B, the differential equation can be obtained as

$$\tau''_{sQ2} - \Gamma_s{}^2\tau_{sQ2} = \frac{G_{bs}\alpha}{E_h t_h t_{bs}}D(x) - \frac{1}{2}D''(x). \quad \text{(C.12)}$$

The free stresses at the boundaries of the sensor and the host structure can be expressed as

$$\begin{cases}\sigma_{sQ2}(x_1) = 0,\ \sigma_{sQ2}(x_2) = 0,\\ \sigma_{hQ2}(x_1) = 0,\ \sigma_{hQ2}(x_2) = 0.\end{cases} \quad \text{(C.13)}$$

By substituting equations (C.1)–(C.6), (C.9) and (C.11) into equation (C.13), the boundary conditions can be further written as

$$\begin{cases}\tau'_{sQ2}(x_1) = \dfrac{t_{bs}(2B + A)}{8}\dfrac{d^2\gamma_{sL}{}^2}{dx^2}\Big|_{x=x_1} = M,\\ \tau'_{sQ2}(x_2) = \dfrac{t_{bs}(2B + A)}{8}\dfrac{d^2\gamma_{sL}{}^2}{dx^2}\Big|_{x=x_2} = N.\end{cases} \quad \text{(C.14)}$$

Combining equations (C.12) and (C.14), the differential equation can be finally solved as

$$\tau_{sQ2} = C_5 e^{\Gamma_s x} + C_6 e^{-\Gamma_s x} + \int_{x_1}^{x}\frac{1}{\Gamma_s}\left(\frac{G_{bs}\alpha}{E_h t_h t_{bs}}D(\theta) - \frac{1}{2}D''(\theta)\right) \times \sinh(\Gamma_s(x - \theta))d\theta, \quad \text{(C.15)}$$

where

$$C_5 = \frac{Me^{\Gamma_s x_1} - Ne^{\Gamma_s x_2} + e^{\Gamma_s x_2}\int_{x_1}^{x_2}\left(\frac{G_{bs}\alpha}{E_h t_h t_{bs}}D(\theta) - \frac{1}{2}D''(\theta)\right)\cosh(\Gamma_s(x_2 - \theta))d\theta}{\Gamma_s(e^{2\Gamma_s x_1} - e^{2\Gamma_s x_2})},$$

$$C_6 = e^{2\Gamma_s x_1}\frac{Me^{\Gamma_s x_1} - Ne^{\Gamma_s x_2} + e^{\Gamma_s x_2}\int_{x_1}^{x_2}\left(\frac{G_{bs}\alpha}{E_h t_h t_{bs}}D(\theta) - \frac{1}{2}D''(\theta)\right)\cosh(\Gamma_s(x_2 - \theta))d\theta}{\Gamma_s(e^{2\Gamma_s x_1} - e^{2\Gamma_s x_2})} - \frac{M}{\Gamma_s}e^{\Gamma_s x_1}. \quad \text{(C.16)}$$

References

[1] Giurgiutiu V 2007 *Structural Health Monitoring: With Piezoelectric Wafer Active Sensors* (New York: Academic)

[2] Chang F K, Markmiller J F C, Yang J and Kim Y 2011 Structural health monitoring *System Health Managment: With Aerospace Applications* (Wiley) pp 419–28

[3] Zhao X, Gao H, Zhang G, Ayhan B, Yan F and Kwan C 2007 Active health monitoring of an aircraft wing with embedded piezoelectric sensor/actuator network: I. Defect detection, localization and growth monitoring *Smart Mater. Struct.* **16** 1208

[4] Raghavan A and Cesnik C E 2007 Review of guided-wave structural health monitoring *Shock Vib.* **39** 91–116

[5] Rose J L 2004 *Ultrasonic Waves in Solid Media* (Cambridge: Cambridge University Press)
[6] Shan S, Qiu J, Zhang C, Ji H and Cheng L 2016 Multi-damage localization on large complex structures through an extended delay-and-sum based method *Struct. Health Monit.* **15** 50–64
[7] Su Z, Ye L and Lu Y 2006 Guided Lamb waves for identification of damage in composite structures: a review *J. Sound Vib.* **295** 3753–80
[8] Masserey B and Fromme P 2013 Fatigue crack growth monitoring using high-frequency guided waves *Struct. Health Monit.* **12** 484–93
[9] Amjad U, Yadav S K and Kundu T 2015 Detection and quantification of pipe damage from change in time of flight and phase *Ultrasonics* **62** 223–36
[10] Su Z, Zhou C, Hong M, Cheng L, Wang Q and Qing X 2014 Acousto-ultrasonics-based fatigue damage characterization: linear versus nonlinear signal features *Mech. Syst. Signal Process.* **45** 225–39
[11] Chillara V K and Lissenden C J 2016 Review of nonlinear ultrasonic guided wave nondestructive evaluation: theory, numerics, and experiments *Opt. Eng.* **55** 011002
[12] Matlack K, Kim J, Jacobs L and Qu J 2015 Review of second harmonic generation measurement techniques for material state determination in metals *J. Nondestruct. Eval.* **34** 1–23
[13] Broda D, Staszewski W, Martowicz A, Uhl T and Silberschmidt V 2014 Modelling of nonlinear crack-wave interactions for damage detection based on ultrasound—a review *J. Sound Vib.* **333** 1097–118
[14] Lim H J, Sohn H and Liu P 2014 Binding conditions for nonlinear ultrasonic generation unifying wave propagation and vibration *Appl. Phys. Lett.* **104** 214103
[15] Deng M 2003 Analysis of second-harmonic generation of Lamb modes using a modal analysis approach *J. Appl. Phys.* **94** 4152–9
[16] Srivastava A and di Scalea F L 2009 On the existence of antisymmetric or symmetric Lamb waves at nonlinear higher harmonics *J. Sound Vib.* **323** 932–43
[17] Liu Y, Chillara V K and Lissenden C J 2013 On selection of primary modes for generation of strong internally resonant second harmonics in plate *J. Sound Vib.* **332** 4517–28
[18] Chillara V K and Lissenden C J 2012 Interaction of guided wave modes in isotropic weakly nonlinear elastic plates: higher harmonic generation *J. Appl. Phys.* **111** 124909
[19] De Lima W and Hamilton W 2003 Finite-amplitude waves in isotropic elastic plates *J. Sound Vib.* **265** 819–39
[20] Lissenden C, Liu Y, Choi G and Yao X 2014 Effect of localized microstructure evolution on higher harmonic generation of guided waves *J. Nondestruct. Eval.* **33** 178–86
[21] Hong M, Su Z, Wang Q, Cheng L and Qing X 2014 Modeling nonlinearities of ultrasonic waves for fatigue damage characterization: theory, simulation, and experimental validation *Ultrasonics* **54** 770–8
[22] Rauter N and Lammering R 2014 Experimental investigation of fatigue damage in composite structures considering second harmonic Lamb waves *EWSHM-7th European Workshop on Structural Health Monitoring*
[23] Wan X, Tse P, Xu G, Tao T and Zhang Q 2016 Analytical and numerical studies of approximate phase velocity matching based nonlinear S0 mode Lamb waves for the detection of evenly distributed microstructural changes *Smart Mater. Struct.* **25** 045023
[24] Yelve N P, Mitra M and Mujumdar P 2014 Higher harmonics induced in lamb wave due to partial debonding of piezoelectric wafer transducers *NDT & E Int.* **63** 21–7
[25] Agrahari J and Kapuria S 2016 Effects of adhesive, host plate, transducer and excitation parameters on time reversibility of ultrasonic Lamb waves *Ultrasonics* **70** 147–57
[26] Sohn H 2007 Effects of environmental and operational variability on structural health monitoring *Phil. Trans. R. Soc.* A **365** 539–60
[27] Ha S and Chang F-K 2010 Adhesive interface layer effects in PZT-induced Lamb wave propagation *Smart Mater. Struct.* **19** 025006
[28] Pruell C, Kim J-Y, Qu J and Jacobs L J 2009 Evaluation of fatigue damage using nonlinear guided waves *Smart Mater. Struct.* **18** 035003
[29] Lanza di Scalea F, Matt H and Bartoli I 2007 The response of rectangular piezoelectric sensors to Rayleigh and Lamb ultrasonic waves *J. Acoust. Soc. Am.* **121** 175
[30] Jin C, Wang X D and Zuo M J 2009 The dynamic behaviour of surface-bonded piezoelectric actuators with debonded adhesive layers *Acta Mech.* **211** 215–35
[31] Giurgiutiu V 2005 Tuned Lamb wave excitation and detection with piezoelectric wafer active sensors for structural health monitoring *J. Int. Mater. Syst. Struct.* **16** 291–305
[32] Chillara V K and Lissenden C J 2014 Nonlinear guided waves in plates: a numerical perspective *Ultrasonics* **54** 1553–8
[33] Nienwenhui J, Neumann J J Jr, Greve D W and Oppenheim I J 2005 Generation and detection of guided waves using PZT wafer transducers *IEEE Trans. Ultrason. Ferr.* **52** 2103–11
[34] http://fujicera.co.jp/product/e/01/mat.table_e.pdf
[35] Choi G, Liu Y, Lissenden C J and Rose J 2014 Influence of localized microstructure evolution on second harmonic generation of guided waves *40th Annual Review of Progress In Quantitative Nondestructive Evaluation: Incorporating the 10th Int. Conf on Barkhausen Noise and Micromagnetic Testing* (AIP Publishing)
[36] Ha S, Lonkar K, Mittal A and Chang F K 2010 Adhesive layer effects on PZT-induced lamb waves at elevated temperatures *Struct. Health Monit.* **9** 247–56
[37] Kim C 2012 Creep damage characterization of Ni-based superalloy by acoustic nonlinearity *Prog. Nat. Sci.* **22** 303–10
[38] http://ni.com/pdf/products/us/2004_4600_305_101_DLR.pdf
[39] http://ni.com/datasheet/pdf/en/ds-239
[40] http://ciprian.com/docs/specifications%20USTXP3%20High%20Speed%20Linear%20Power%20Amplifier%20Ciprian%20v1.6.pdf